Available online at www.sciencedirect.com
ScienceDirect
International Journal of Multiphase Flow 34 (2008) 283–302
International Journal of Multiphase Flow
www.elsevier.com/locate/ijmulflow

Combined multi-direct forcing and immersed boundary method for simulating flows with moving particles

Zeli Wang, Jianren Fan *, Kun Luo

State Key Laboratory of Clean Energy Utilization (Zhejiang University), Hangzhou 310027, PR China

Received 8 February 2007; received in revised form 11 September 2007

Abstract

Accurate description of particle–fluid interaction is one of the big challenges in the community of multiphase flows. Toward this direction, the combined multi-direct forcing and immersed boundary method were presented to simulate flows laden with finite-size moving particles with full-scale solutions. In the approach, the hydrodynamic interactions between moving rigid boundary and fluid were calculated using the *multi-direct forcing* scheme. The no-slip boundary conditions at the immersed boundaries can be satisfied well in this way. Direct numerical simulations of particle sedimentation under various conditions were performed based on the multi-direct forcing scheme, the immersed boundary method and the high-order finite difference. It is proved that this approach can successfully simulate the interactions between fluid and particle, the interactions between particle and particle as well as the interactions between particles and wall. The hitting and rebounding process of the single particle sedimentation, the drafting–kissing–tumbling of two settling particles and many particles sedimentation were observed. The quantitative comparisons against other studies were also conducted to validate the present approach.

Keywords: Direct numerical simulation; Multi-direct forcing; Immersed boundary method; Particle sedimentation; Interactions between fluid and particle

1. Introduction

Matter commonly occurs in one of three phases, namely solid, liquid and gas. Any flow involving two or three phases is a multiphase flow. Multiphase flows exist widely both in nature and in industry, including atmospheric currents, dust storms, spray combustion, aerosol deposition, pollutants transport and so on. Almost 90% flows are multiphase flows. In multiphase flows, the inter-phase interactions are one of the key problems, which greatly influence the heat and mass transfer in the flows. Thus, the inter-phase interactions in multiphase flows have attracted lots of researcher's attention in the past decades (Tsuji and Morikawa, 1982; Tsuji et al., 1984; Gore and Crowe, 1989; Hetsroni, 1989; Pan et al., 2002).

Compared to experimental measurements, the numerical simulations have remarkable advantages in exploring the inter-phase interactions in multiphase flows because the boundary conditions and impact parameters can be separately studied. But the results of the numerical simulations should be credible. Therefore, developing of numerical methods with higher accuracy is of great significance to effectively simulate multiphase flows. Currently, the highest-resolution numerical method for turbulence simulation is direct numerical simulation (DNS). Although it is limited to study the flows with low Reynolds numbers, great achievements have been obtained (Moin and Mahesh, 1998). While for multiphase flows, there are two kinds of DNS approaches with different levels at present. In the first level approach, the particle is considered as real finite volume and the hydrodynamic force acted on the particle is accurately calculated by integrating the viscosity and pressure forces imposed by fluid. In this approach, both

* Corresponding author. Tel.: +86 571 87951764.
E-mail address: fanjr@zju.edu.cn (J. Fan).

0301-9322/$ - see front matter © 2007 Elsevier Ltd. All rights reserved.
doi:10.1016/j.ijmultiphaseflow.2007.10.004

the fluid and the particle are simulated using DNS. The particle size can be larger than the grid size and there is no any empirical model is introduced. The flow around the particle, such as the wake can also be captured. From this point of view, this level method is the fully resolved or truly direct numerical simulation of multiphase flows. In the second level approach, the fluid is simulated using DNS, but the particle is assumed to be a mass point without volume and the main force acted on it is modeled by the Stokes drag force. This method is available when the particle scale is smaller than the grid scale and the flow is dilute. It belongs to the traditional DNS of multiphase flows and has been extensively applied in the past decades (Squires and Eaton, 1990; Pedinotti et al., 1992; Ling et al., 1998; Soltani et al., 1998; Barré et al., 2001; Marchioli et al., 2003; Ferrante and Elghobashi, 2003; Fan et al., 2004; Biswas et al., 2005; Luo et al., 2006).

Simulations of the interaction between particle and fluid with high accuracy are difficult. The major challenge is how to deal with the boundary between particle and fluid. Due to its unique advantages, the fully resolved DNS method has become popular and popular, and many numerical schemes have been developed in the past 15 years. Hu and co-workers (1996, 2001) proposed the boundary fitted techniques to simulate fluid particle motions. The finite element methods based on unstructured grids were used. Some microcosmic phenomena and mechanisms were successfully observed. However, the adapting mesh to the varying positions of the particles during the simulation leads to tremendous computational cost. In order to avoid the time-consuming re-meshing, a series of methods based on a fixed Cartesian grid were put forward to simulate flows with complex boundary. Glowinski et al. (1999, 2001) presented a distributed Lagrange multiplier/fictitious domain method for particulate flows, which consists to fill the moving bodies by the surrounding fluid and impose a rigid body motion to the fluid filling the regions previously occupied by the rigid bodies and then the rigid body motion constraint can be relaxed by using distributed Lagrange multipliers. The advantages of this method are that one does not need to generate new mesh and to calculate the hydrodynamic forces at each time step. Patankar et al. (2000) improved this method by presenting a new DLM formulation to impose the rigid motion by constraining the deformation-rate tensor within the particle domain to be zero. Recently, they have also introduced the fast computation technique for direct numerical simulation of particulate flows (Sharma and Patankar, 2005). The above ALE and DLM formulations have been implemented for various laminar and small density-ratio solid–liquid flow conditions (Pan et al., 2001, 2002; Patankar and Joseph, 2001; Patankar et al., 2002; Singh et al., 2003; Cho et al., 2005). Ladd and Verberg (2001) developed the Lattice Boltzmann method (LBM) to simulate particulate suspensions. Maxey and Patel (2001) proposed the force-coupling method (FCM) for particulate flows. This method is based on representing the particles by low-order force multipoles distributed over a finite volume. They found that the DNS results are in good agreement with their experimental data when the particle Reynolds number is small (Lomholt et al., 2002). Burton and Eaton (2005) performed fully resolved simulations of the particle–turbulence interaction by using the overset grid method. They found that the real force imposed on particle is largely different from that computed based on the standard Stokes drag expression. Prosperetti and Oguz (2001) presented a new approach, Physalis, to the direct numerical simulation of potential problems with many spherical internal boundaries. The basic idea is to use a local analytic representation valid near the particle to transfer the no-slip condition from the particle surface to the adjacent grid nodes. Thus the irregular relation between the particle boundary and the underlying mesh is avoided and fast solvers can be used. This method was also successfully extended to simulate two-dimensional Navier–Stokes flow around cylinders and moving particles (Takagi et al., 2003; Zhang and Prosperetti, 2003). At the same time, the volume-of-fluid method (Scardovelli and Zaleski, 1999), the level set method (Sussman et al., 1994), the constrained interpolation profile method (Yabe et al., 2001) and the front tracking method (Tryggvason et al., 2001) have also been presented to simulate the liquid–liquid or gas–liquid two-phase flows.

In particular, the immersed boundary method (IBM), originally developed by Peskin (1972) has attracted considerable interest in the last few years (Mittal and Iaccarino, 2005). In Peskin's case, the singular force on the Lagrangian coordinates of the boundary was exerted on the flow flied which is on the Eulerian coordinates via a regularized Dirac delta function. To calculate the interactions between solid boundary and fluid, Goldstein et al. (1993) proposed a feedback scheme to iteratively determine the magnitude of the force required to obtain a desired velocity on the immersed boundary. The feedback forcing is in the form:

$$\boldsymbol{f}(\boldsymbol{x}_s,t) = \alpha \cdot \int_0^t [\boldsymbol{u}(\boldsymbol{x}_s,t') - \boldsymbol{V}(\boldsymbol{x}_s,t')]\,\mathrm{d}t' + \beta \cdot [\boldsymbol{u}(\boldsymbol{x}_s,t) - \boldsymbol{V}(\boldsymbol{x}_s,t)] \tag{1}$$

where α and β are negative constants, $\boldsymbol{u}(\boldsymbol{x}_s,t)$ is the fluid velocity at surface point $\boldsymbol{x}_s$, and $\boldsymbol{V}(\boldsymbol{x}_s,t)$ is the velocity of the body boundary itself.

The above formulation is a feedback to the velocity difference $\boldsymbol{u}(\boldsymbol{x}_s,t) - \boldsymbol{V}(\boldsymbol{x}_s,t)$ and it will enforce $\boldsymbol{u}(\boldsymbol{x}_s,t) = \boldsymbol{V}(\boldsymbol{x}_s,t)$ on the immersed boundary. Saiki and Biringen (1996) implemented this feedback scheme to compute the flow past a circular cylinder with virtual boundary method (VBM) successfully. In their work, the boundary of the circular cylinder is composed of more than one thousand Lagrangian points and through extrapolation scheme the feedback forcing which exerts on the Lagrangian point can affect the fluid that around the circular cylinder. In order to let the velocity at the boundary of the circular cylinder satisfy the no-slip boundary, a proper choose of the

tow negative constants α and β which can lead to different feedback forcing should be done. Under the effect of the feedback forcing, the velocity on each Lagrangian point trends to zero after a period of time that means the feedback forcing can not let the velocity at the immersed boundary satisfy the no-slip boundary condition immediately.

On the other hand, Fadlun et al. (2000) proposed an approach to calculate the interaction force between immersed boundary and fluid which is called direct forcing based on immersed boundary method. The velocity at the points which are close to the immersed boundary is simply set at every time step. It seems like applying an equivalent forcing term to the Navier–Stokes equations. Compared with the feedback forcing, the direct forcing is more general because there is not any unknown constant that should be determined in the formulation of solving direct forcing. However, under the effect of direct forcing, the velocity at the points on the immersed boundary may not effectively satisfy the no-slip boundary condition due to the mutual influence of the direct forcing at the neighboring points.

In order to overcome the problem, a new *multi-direct forcing* technique with the immersed boundary method is proposed in present paper for the simulation of flows laden with moving particles. This scheme can let the velocity at the immersed boundary trend to satisfy the no-slip boundary immediately and accurately. We will present the method to combine the IBM's ability to smoothly transfer quantities between Lagrangian and Eulerian points with the advantages of multi-direct formulation of the fluid–solid interactions.

2. Mathematic description

2.1. Governing equations for fluid flow

The dimensionless governing equations for incompressible flows in the entire computational domain Ω are:

$$\nabla \cdot \boldsymbol{u} = 0 \tag{2}$$

$$\frac{\partial \boldsymbol{u}}{\partial t} + \boldsymbol{u} \cdot \nabla \boldsymbol{u} = -\nabla P + \frac{1}{Re}\nabla^2 \boldsymbol{u} + \boldsymbol{f} \tag{3}$$

where $\boldsymbol{u}$ is the velocity of fluid, P is the pressure and Re is the Reynolds number defined as $Re = \frac{\rho \cdot U \cdot L}{\mu}$. Here ρ is the density of fluid, U is the characteristic velocity of flow field, L is the characteristic length of flow field and μ is the viscosity of fluid. $\boldsymbol{f}$ in Eq. (3) is the external force exerted on the flow field which is the mutual interaction force between fluid and immersed boundary expressed as following:

$$\boldsymbol{f}(\boldsymbol{x}) = \int_{\Omega} \boldsymbol{F}_k(\boldsymbol{x}_k) \cdot \delta(\boldsymbol{x} - \boldsymbol{x}_k) \mathrm{d}\boldsymbol{x}_k \tag{4}$$

where $\delta(\boldsymbol{x} - \boldsymbol{x}_k)$ is the Dirac delta function, $\boldsymbol{x}_k$ is the position of the Lagrangian points set at the immersed boundary, $\boldsymbol{x}$ is position of the computational Eulerian mesh and $\boldsymbol{F}_k(\boldsymbol{x}_k)$ is the force exerted on the Lagrangian point $\boldsymbol{x}_k$.

2.2. Schemes of multi-direct forcing

In order to let the velocity on the Lagrangian points at the immersed boundary satisfy the no-slip boundary condition, a forcing $\boldsymbol{F}_k(\boldsymbol{x}_k)$ is imposed on the Lagrangian point to modify its velocity equal the desired velocity $\boldsymbol{u}_L$ at the immersed boundary. The forcing $\boldsymbol{F}_k(\boldsymbol{x}_k)$ is determined as follows:

From the above Eq. (3), one can get

$$\begin{aligned}\boldsymbol{f} &= \frac{\partial \boldsymbol{u}}{\partial t} + \boldsymbol{u} \cdot \nabla \boldsymbol{u} + \nabla P - \frac{1}{Re}\nabla^2 \boldsymbol{u} = \frac{\partial \boldsymbol{u}}{\partial t} - \boldsymbol{rhs} \\ &= \frac{\boldsymbol{u}^{n+1} - \boldsymbol{u}^n}{\Delta t} - \boldsymbol{rhs}\end{aligned} \tag{5}$$

where n and $n+1$ represent two different times and

$$\boldsymbol{rhs} = -\left(\boldsymbol{u} \cdot \nabla \boldsymbol{u} + \nabla P - \frac{1}{Re}\nabla^2 \boldsymbol{u}\right). \tag{6}$$

For the Lagrangian point $\boldsymbol{x}_k$ at the immersed boundary, one can get

$$\boldsymbol{F}_k(\boldsymbol{x}_k) = \frac{\boldsymbol{u}_k^{n+1} - \boldsymbol{u}_k^n}{\Delta t} - \boldsymbol{rhs}_k = \frac{\boldsymbol{u}_k^{n+1} - \hat{\boldsymbol{u}}_k}{\Delta t} + \frac{\hat{\boldsymbol{u}}_k - \boldsymbol{u}_k^n}{\Delta t} - \boldsymbol{rhs}_k \tag{7}$$

where $\hat{\boldsymbol{u}}_k$ is a temporary parameter which satisfies the momentum equation that is

$$\frac{\hat{\boldsymbol{u}}_k - \boldsymbol{u}_k^n}{\Delta t} - \boldsymbol{rhs}_k = 0 \tag{8}$$

and

$$\boldsymbol{rhs}_k = -\left(\boldsymbol{u} \cdot \nabla \boldsymbol{u} + \nabla P - \frac{1}{Re}\nabla^2 \boldsymbol{u}\right)_k \tag{9}$$

Therefore, the forcing exerted on the Lagrangian points at the immersed boundary is

$$\boldsymbol{F}_k(\boldsymbol{x}_k) = \frac{\boldsymbol{u}_k^{n+1} - \hat{\boldsymbol{u}}_k}{\Delta t} = \frac{\boldsymbol{u}_L - \hat{\boldsymbol{u}}_k}{\Delta t} \tag{10}$$

Under the effect of the forcing, the velocity on the Lagrangian point $\boldsymbol{x}_k$ at $n+1$ time $\boldsymbol{u}_k^{n+1}$ can be modified to the desired velocity $\boldsymbol{u}_L$. The forcing is direct in the sense that the desired value of velocity is imposed directly on the boundary without any dynamical process (Fadlun et al., 2000) and the forcing is based upon the law of conservation (Silva et al., 2003).

The Dirac delta function is applied to spread the two-way coupling between Eulerian girds and Lagrangian points. The temporary velocity on the Lagrangian point at the immersed boundary $\boldsymbol{x}_k$ is obtained from its surrounding Eulerian grids $\boldsymbol{x}$.

$$\hat{\boldsymbol{u}}_k = \sum_{x \in \Omega} \hat{\boldsymbol{u}} \cdot \delta_h(\boldsymbol{x}_k - \boldsymbol{x}) \cdot h^2 \tag{11}$$

where $\hat{\boldsymbol{u}}$ is also the temporary parameter on the Eulerian grids which satisfies the momentum equation that is:

$$\frac{\hat{\boldsymbol{u}} - \boldsymbol{u}^n}{\Delta t} - \boldsymbol{rhs} = 0 \tag{12}$$

The effect of the forcing on the Lagrangian points which spreads into the Eulerian grids is expressed as:

$$\begin{aligned} \boldsymbol{f}(\boldsymbol{x}) &= \int_{\Omega} \boldsymbol{F}_k(\boldsymbol{x}_k)\cdot\delta(\boldsymbol{x}-\boldsymbol{x}_k)\mathrm{d}\boldsymbol{x}_k \\ &= \sum_{k=1}^{N} \boldsymbol{F}_k(\boldsymbol{x}_k)\cdot\delta_h(\boldsymbol{x}-\boldsymbol{x}_k)\cdot\Delta V_k \end{aligned} \tag{13}$$

where N is the number of Lagrangian points, and ΔV_k is the discrete volume for each Lagrangian point.

The discrete delta function is chosen as that of Griffith and Peskin (2005)

$$\delta_h(\boldsymbol{x}-\boldsymbol{x}_k) = \frac{1}{h^2} d_h\left(\frac{x-x_k}{h}\right)\cdot d_h\left(\frac{y-y_k}{h}\right) \tag{14}$$

where $\boldsymbol{x}=(x,y)$, $\boldsymbol{x}_k=(x_k, y_k)$, h is the Eulerian mesh size, and

$$d_h(r) = \begin{cases} \frac{1}{8}(3-2|r|+\sqrt{1+4|r|-4r^2}) & 0\leqslant|r|<1 \\ \frac{1}{8}(5-2|r|-\sqrt{-7+12|r|-4r^2}) & 1\leqslant|r|<2 \\ 0 & 2\leqslant|r| \end{cases} \tag{15}$$

To solve the governing equations, the spatial derivatives are discretized using the fourth-order compact finite difference scheme (Lele, 1992) based on non-staggered grid. The pressure-Poisson equation derived by applying the divergence operator to the momentum equations replaces the continuity equation that is satisfied indirectly through the solution of the pressure equation. To reduce the cost of core memory in simulations, a four-step-four-order Runge–Kutta marching scheme (Jameson and Schmidt, 1985) is applied to the time integration. The computational algorithm is described as follows:

$$\boldsymbol{u}^{l+1} = \boldsymbol{u}^n + \boldsymbol{rhs}^l\cdot\frac{\Delta t}{4-l} \quad l=0,1,2,3 \tag{16}$$

$$\hat{\boldsymbol{u}}_k = \sum_{x\in\Omega}\boldsymbol{u}^4\cdot\delta(\boldsymbol{x}_k-\boldsymbol{x})\cdot h^2 \tag{17}$$

$$\boldsymbol{F}_k(\boldsymbol{x}_k) = \frac{\boldsymbol{u}_L-\hat{\boldsymbol{u}}_k}{\Delta t} \tag{18}$$

$$\boldsymbol{f}(\boldsymbol{x}) = \sum_{k=1}^{N}\boldsymbol{F}_k(\boldsymbol{x}_k)\cdot\delta(\boldsymbol{x}-\boldsymbol{x}_k)\cdot\Delta V_k \tag{19}$$

$$\boldsymbol{u}^{n+1} = \boldsymbol{u}^4 + \boldsymbol{f}(\boldsymbol{x})\cdot\Delta t \tag{20}$$

$$\nabla^2 P = -\nabla\cdot(\boldsymbol{u}\cdot\nabla\boldsymbol{u}) - \frac{\partial D}{\partial t} + \nabla\cdot\boldsymbol{f} \tag{21}$$

where $\Delta V_k = \frac{2\cdot\pi\cdot r}{N}\cdot h$ is proposed by Uhlmann (2005) and $D=\nabla\cdot\boldsymbol{u}$.

The above direct forcing exerted on the Lagrangian point $\boldsymbol{x}_k$ can modify the computational velocity $\hat{\boldsymbol{u}}_k$ to the desired velocity $\boldsymbol{u}_L$. However, when spreading the effect of forcing from the Lagrangian points to the Eulerian grids, different schemes of discrete delta function can lead to different results. And the velocities on the Lagrangian points may not satisfy the no-slip boundary condition very well during the process of interpolation to obtain the simulated velocity on the Lagrangian points and extrapolation to spread the forcing effect to its surrounding Eulerian grids. Therefore, the *multi-direct forcing* technique described as below is applied here.

By solving Eqs. (16)–(20), the velocity of the whole flow field $\boldsymbol{u}_1^{n+1}$ is obtained where $n+1$ is the time level and the under subscript 1 represents exerting the direct forcing for the first time. Then the velocity on the Lagrangian point is

$$\hat{\boldsymbol{u}}_k^1 = \sum_{x\in\Omega}\boldsymbol{u}_1^{n+1}\cdot\delta(\boldsymbol{x}_k-\boldsymbol{x})\cdot h^2 \tag{22}$$

The best result is $\hat{\boldsymbol{u}}_k^1=\boldsymbol{u}_L$, but always $\hat{\boldsymbol{u}}_k^1\neq\boldsymbol{u}_L$. Though the velocity at the immersed boundary can get close to the desired velocity after a long period of time, the no-slip boundary condition is still not satisfied very well. For the sake of getting the velocity on the Lagrangian point much close to the desired velocity, the direct forcing is exerted for the second time which makes

$$\boldsymbol{F}_k^2(\boldsymbol{x}_k) = \frac{\boldsymbol{u}_L-\hat{\boldsymbol{u}}_k^1}{\Delta t} \tag{23}$$

Then the forcing is spread from the Lagrangian points to the Eulerian grids through the Dirac delta function

$$\boldsymbol{f}^2(\boldsymbol{x}) = \sum_{k=1}^{N}\boldsymbol{F}_k^2(\boldsymbol{x}_k)\cdot\delta(\boldsymbol{x}-\boldsymbol{x}_k)\cdot\Delta V_k \tag{24}$$

After exerting the direct forcing for the second time, the velocity of the whole flow field becomes

$$\boldsymbol{u}_2^{n+1} = \boldsymbol{u}_1^{n+1} + \boldsymbol{f}^2(\boldsymbol{x})\cdot\Delta t \tag{25}$$

Thus the velocity on the Lagrangian point at the immersed boundary becomes

$$\hat{\boldsymbol{u}}_k^2 = \sum_{x\in\Omega}\boldsymbol{u}_2^{n+1}\cdot\delta(\boldsymbol{x}_k-\boldsymbol{x})\cdot h^2 \tag{26}$$

The value of $\hat{\boldsymbol{u}}_k^2$ is expected to be closer to the desired velocity $\boldsymbol{u}_L$ than that of $\hat{\boldsymbol{u}}_k^1$. After NF times of this procedure during one time step, the velocity at the immersed boundary can get much close to the desired velocity. The total forcing exerting on each Lagrangian point $F_k(\boldsymbol{x}_k)$ is the sum of the forcing exerting on each Lagrangian point for the whole NF times, that is:

$$F_k(\boldsymbol{x}_k) = \sum_{i=1}^{NF}F_k^i(\boldsymbol{x}_k) \tag{27}$$

In the present study, the multi-direct forcing technique is applied to simulate flows with moving particles. The main advantage of the multi-direct forcing technique is that under the effect of multi-direct forcing, the no-slip boundary condition on the Lagrangian points at the immersed boundary can be well satisfied immediately and accurately when using the immersed boundary method proposed by Peskin (1972) for the simulation of particulate flows.

2.3. Governing equations for particle motion

Based on the above direct-forcing scheme and immersed boundary method, the force and the torque exerted on a moving particle immersed in the incompressible flows can be expressed as

$$\boldsymbol{F} = -\int_1^N \boldsymbol{F}_k(\boldsymbol{x}_k)\mathrm{d}\boldsymbol{s} = -\int_\Omega \boldsymbol{f}(\boldsymbol{x})\mathrm{d}\boldsymbol{x} = -\sum_{x\in\Omega}\boldsymbol{f}(\boldsymbol{x})h^2 \tag{28}$$

$$\begin{aligned}\boldsymbol{T} &= -\int_1^N (\boldsymbol{x}_k-\boldsymbol{x}_c)\times\boldsymbol{F}_k(\boldsymbol{x}_k)\mathrm{d}\boldsymbol{s} = -\int_\Omega (\boldsymbol{x}-\boldsymbol{x}_c)\times\boldsymbol{f}(\boldsymbol{x})\mathrm{d}\boldsymbol{x}\\ &= -\sum_{x\in\Omega}(\boldsymbol{x}-\boldsymbol{x}_c)\times\boldsymbol{f}(\boldsymbol{x})h^2\end{aligned} \tag{29}$$

where $\boldsymbol{x}_c$ is the center of the particle.

Then the motion of the particle is governed by the following equations:

$$M\frac{\mathrm{d}\boldsymbol{U}}{\mathrm{d}t} = M\boldsymbol{g} + \boldsymbol{F} + \boldsymbol{F}' \tag{30}$$

$$\frac{\mathrm{d}\boldsymbol{X}}{\mathrm{d}t} = \boldsymbol{U} \tag{31}$$

$$I\frac{\mathrm{d}\omega}{\mathrm{d}t} = \boldsymbol{T} \tag{32}$$

$$\frac{\mathrm{d}\boldsymbol{\theta}}{\mathrm{d}t} = \omega \tag{33}$$

where M is the mass of particle, $\boldsymbol{U}$ is the velocity of particle, $\boldsymbol{g}$ is the gravitational acceleration, X is the center of particle, I is the moment of inertia, $\boldsymbol{\omega}$ is the angular velocity, $\boldsymbol{\theta}$ is the angular orientation of the particle and $\boldsymbol{F}'$ is the collision force acting on the particle by other particles and the wall when they come close to each other.

The desired velocity on the Lagrangian point at the immersed boundary is

$$\boldsymbol{u}_L = \boldsymbol{U} + \boldsymbol{\omega}\times(\boldsymbol{x}_k - \boldsymbol{x}_c) \tag{34}$$

The discretization forms of the governing equations are summarized as follows:

$$\boldsymbol{U}^{n+1} = \boldsymbol{U}^n + \frac{(\boldsymbol{F}^n + \boldsymbol{F}'^n)}{M}\Delta t + \boldsymbol{g}\cdot\Delta t \tag{35}$$

$$\boldsymbol{X}^{n+1} = \boldsymbol{X}^n + \frac{\boldsymbol{U}^n + \boldsymbol{U}^{n+1}}{2}\Delta t \tag{36}$$

$$\boldsymbol{\omega}^{n+1} = \boldsymbol{\omega}^n + \frac{\boldsymbol{T}^n}{M}\Delta t \tag{37}$$

$$\boldsymbol{\theta}^{n+1} = \boldsymbol{\theta}^n + \frac{\boldsymbol{\omega}^n + \boldsymbol{\omega}^{n+1}}{2}\Delta t \tag{38}$$

When spreading the effect of the forcing from the Lagrangian points to the Eulerian nodes with multi-direct forcing scheme, the force acted on the Lagrangian point which contains the desired velocity $\boldsymbol{u}_L$ and the simulated velocity $\hat{\boldsymbol{u}}_k^i$ (i represents the ith time of exerting the direct forcing) should be calculated by using Eqs. (19) and (24). However, the desired velocity at $n+1$ time level $\boldsymbol{u}_L^{n+1}$ is unknown. A simple way to deal with it is applying a one-order explicit scheme with $\boldsymbol{u}_L^n$ instead of $\boldsymbol{u}_L^{n+1}$. This way has been used in previous numerical simulations (Kajishima and Takiguchi, 2002; Wan and Turek, 2007). For the sake of convenience, we also use this explicit scheme in the present study. Then the force exerted on the Lagrangian point at the immersed boundary should be changed as

$$\boldsymbol{F}_k(\boldsymbol{x}_k) = \frac{\boldsymbol{u}_L^{n+1} - \hat{\boldsymbol{u}}_k}{\Delta t} \approx \frac{\boldsymbol{u}_L^n - \hat{\boldsymbol{u}}_k}{\Delta t} \tag{39}$$

where $\boldsymbol{u}_L^n = \boldsymbol{U}^n + \boldsymbol{\omega}^n\times(\boldsymbol{x}_k^n - \boldsymbol{x}_c^n)$.

2.4. Particle–particle collision

A collision model is applied in present numerical simulation to prevent the particles from interpenetration each other. Glowinski et al. (1999) proposed a short-range repulsive force model to keep the distance between particulate surfaces more than one element. Singh et al. (2003) suggested a modified repulsive force model which allows a little overlap of each particle. Wan and Turek (2007) combined the two models to simulate the collision between particles. In the present simulations, the combined repulsive model is also used to deal with the particle–particle collision.

For particle–particle collisions, the repulsive force is determined as:

$$\boldsymbol{F}_{i,j}^P = \begin{cases} \frac{1}{\varepsilon_\mathrm{P}}(\boldsymbol{X}_i - \boldsymbol{X}_j)(R_i + R_j - d_{i,j}) & d_{i,j} < R_i + R_j \\ \frac{1}{\varepsilon_\mathrm{P}}(\boldsymbol{X}_i - \boldsymbol{X}_j)(R_i + R_j + \xi - d_{i,j})^2 & R_i + R_j \leqslant d_{i,j} < R_i + R_j + \xi \\ 0 & R_i + R_j + \xi \leqslant d_{i,j} \end{cases} \tag{40}$$

where R_i and R_j are the radius of the ith and the jth particle, $\boldsymbol{X}_i$ and $\boldsymbol{X}_j$ are the centers of the ith and the jth particle, $d_{i,j} = |\boldsymbol{X}_i - \boldsymbol{X}_j|$ is the distance between their center, ξ is the range of the repulsive force, ε_P and ε'_P are small positive stiffness parameters for particle–particle collisions.

For particle–wall collisions, the repulsive force is:

$$\boldsymbol{F}_i^\mathrm{W} = \begin{cases} \frac{1}{\varepsilon'_\mathrm{P}}(\boldsymbol{X}_i - \boldsymbol{X}'_i)(2R_i - d'_i) & d_{i,j} < 2R_i \\ \frac{1}{\varepsilon_\mathrm{P}}(\boldsymbol{X}_i - \boldsymbol{X}'_i)(2R_i + \xi - d'_i)^2 & 2R_i \leqslant d_{i,j} < 2R_i + \xi \\ 0 & 2R_i + \xi \leqslant d_{i,j} \end{cases} \tag{41}$$

where $\boldsymbol{X}'_i$ is the coordinate vector of the center of the nearest imaginary particle located on the boundary.

Then the total collision force exerting on the ith particle by other particles and the walls is:

$$\boldsymbol{F}'_i = \sum_{j=1, j\neq i}^{N} \boldsymbol{F}_{i,j}^P + \boldsymbol{F}_i^\mathrm{W} \tag{42}$$

3. Numerical implementations and discussions

In the present work, we apply the multi-direct forcing technique to simulate two-dimensional flows with moving particles. The sedimentations of single particle, two

particles and up to 105 particles under different conditions are investigated.

3.1. Single particle sedimentation

In this simulation, for convenience of comparison, the computational parameters are chosen as the same as those of Glowinski et al. (2001) and summarized as follows:

The computational domain is $\Omega = (0.2\text{ cm}) \times (0.6\text{ cm})$.
The diameter of the particle is $D_P = 0.25$ cm.
The density of the particle is $\rho_P = 1.25$ g/cm^3 and 1.5 g/cm^3.
The center of the particle is located at (1 cm, 4 cm) at time $t = 0$ s.
The fluid and the particle are initially at rest.
The fluid density is $\rho_f = 1.00$ g/cm^3.
The fluid viscous is $\mu = 0.1$ g/(cm s) and 0.01 g/(cm s).
The collision parameter is $\varepsilon_W = 0.5 \times 10^{-6}$.

The mesh sizes are set as $\frac{1}{18}$, $\frac{1}{36}$ and $\frac{1}{64}$ of the particulate diameter and the corresponding mesh sizes are $h = \frac{1}{72}$ cm, $h = \frac{1}{144}$ cm and $h = \frac{1}{256}$ cm, respectively. And for the three kinds of mesh sizes 57, 114 and 202 Lagrangian points are used at the immersed boundary, respectively.

The maximum Reynolds number is defined as

$$Re_{\text{Max}} = \text{Max}[Re(t)] = \text{Max}\left[\frac{\rho_P \sqrt{U_P(t)^2 + V_P(t)^2} \cdot D_P}{\mu}\right] \tag{43}$$

To examine the effect of multi-direct forcing for particulate flows, the l_{P2}-norm error of the velocities on the Lagrangian points at the immersed boundary with respect to no-slip boundary condition is defined as follows as a parameter and tracked at every time step.

$$l_{P2} = \frac{\sqrt{\frac{\sum_{k=1}^{N}[(u_k - u_L)^2 + (v_k - v_L)^2]}{N}}}{\sqrt{U_P(t)^2 + V_P(t)^2 + (0.5 \cdot \omega(t) \cdot D_p)^2}} \quad \text{when } (U_P(t), V_P(t), \omega(t)) \neq (0,0,0) \tag{44}$$

where $\boldsymbol{U}(t) = (U_P(t), V_P(t))$ is the velocity of mass center of the particle, $\omega(t)$ is the angular velocity for the present two-dimensional flow and D_P is the diameter of particle. This l_{P2}-norm shows the relative error of the velocity at the immersed boundary with respect to the no-slip boundary condition. In the present simulations of particle sedimentation, the velocity of particle almost is not equal to zero. Then the l_{P2}-norm is not tracked when $(U_P(t), V_P(t), \omega(t)) = (0,0,0)$.

The times of performing the multi-direct forcing on each Lagrangian point at the immersed boundary NF is 1, 4, 10 and 20 to check the effect of this multi-direct forcing scheme for single particle sedimentation under the conditions of $\rho_P = 1.25$ g/cm^3, $\mu = 0.1$ g/(cm s), mesh size $h = \frac{1}{256}$ cm and time step $\Delta t = 3.125 \times 10^{-6}$ s. The average value of l_{P2}-norm for different times of multi-directing forcing NF is shown in Fig. 1. When NF is 1 which means that the original direct forcing scheme proposed by Fadlun et al. (2000) is applied, the average value of l_{P2}-norm is 1.4×10^{-4}. When increasing the times of performing the multi-direct forcing NF, the average value of l_{P2}-norm decreases in a "−2" slope manner in the log–log plot. And when NF is 20, the average value of l_{P2}-norm reduces to 1.52×10^{-6} which means a better no-slip boundary condition is reached. This indicates that the multi-direct forcing scheme can improve the no-slip boundary condition at the immersed boundary in comparison with the original direct forcing scheme proposed by Fadlun et al. (2000).

The time history of l_{P2}-norm for single particle sedimentation under the conditions of $\rho_P = 1.25$ g/cm^3, $\mu = 0.1$ g/(cm s), $NF = 20$ mesh size $h = \frac{1}{256}$ cm and time step $\Delta t = 3.125 \times 10^{-6}$ s corresponding to the maximum CFL num-

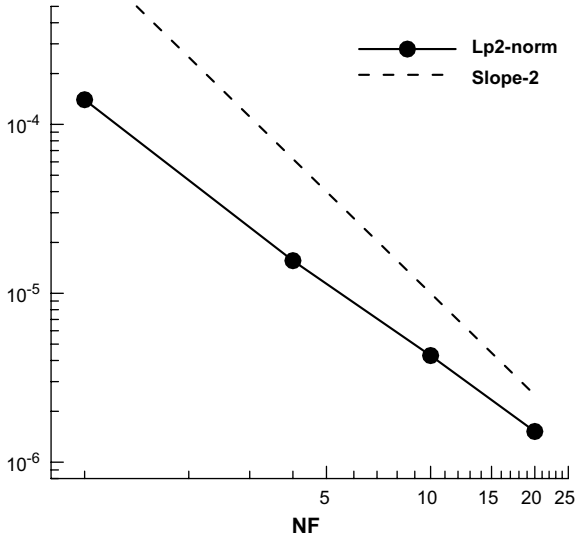

Fig. 1. The average value of l_{P2}-norm for different times of multi-directing forcing ($NF = 1$, 4, 10 and 20) for $\rho_P = 1.25$ g/cm^3, $\mu = 0.1$ g/(cm s), $h = \frac{1}{256}$ cm and $\Delta t = 3.125 \times 10^{-6}$ s.

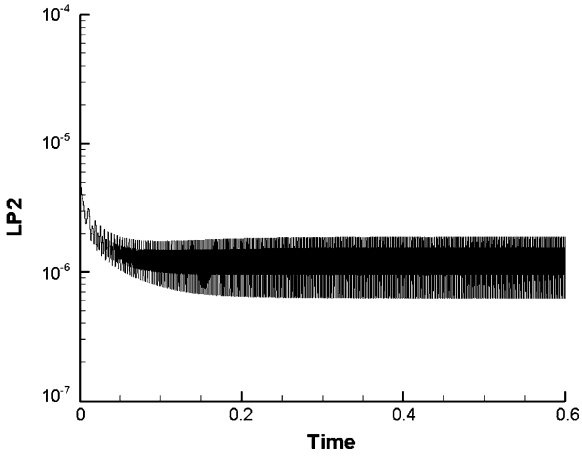

Fig. 2. Time history of l_{P2}-norm for $\rho_P = 1.25$ g/cm^3, $\mu = 0.1$ g/(cm s), $h = \frac{1}{256}$ cm and $\Delta t = 3.125 \times 10^{-6}$ s.

ber 0.0044 is shown in Fig. 2. It can be seen that the l_{P2}-norm reduces to 1.52×10^{-6} in a very short time and maintains this lower level during the whole simulation. This means that the multi-direct forcing scheme can modify the simulated velocity at the immersed boundary to closely approach the desired velocity and the no-slip boundary condition at the Lagrangian points is satisfied well at every time step during the particle settling in the flow field.

The average value of l_{P2}-norm defined in Eq. (44) for three different mesh sizes conditions corresponding to $h=\frac{1}{72}$ cm, $\frac{1}{144}$ cm and $\frac{1}{256}$ cm ($\rho_P=1.25$ g/cm^3, $\mu=0.1$ g/(cm s), $\Delta t=3.125\times10^{-6}$ s, $NF=20$) is shown in Fig. 3. The average value of l_{P2}-norm for $h=\frac{1}{72}$ cm is 5.87×10^{-6} which is a very small number and this indicates that the no-slip boundary at the immersed boundary of the particle is reached very well with the multi-direct forcing technique. And the average value of l_{P2}-norm for $h=\frac{1}{144}$ cm is 3.9×10^{-6}. When changing the resolution of grid, the average value of l_{P2}-norm varies in a "2" slope in the log–log plot.

Table 1 shows the comparison of the maximum Reynolds number during the particle settling in the flow with previous related numerical results. The present predicted maximum Reynolds numbers under different mesh sizes are in good agreement with those of Glowinski et al. (2001) and Wan and Turek (2007). The maximum Reynolds numbers of different temporal increments for $h=\frac{1}{256}$ cm are shown in Table 2. The value of maximum Reynolds numbers are 17.323, 17.316 and 17.307 for $\Delta t=5\times10^{-5}$ s, $\Delta t=6.25\times10^{-6}$ s, and $\Delta t=3.125\times10^{-6}$ s, respectively. And the average value of l_{P2}-norm at different temporal resolutions is shown in Fig. 4. The average value of l_{P2}-norm varies in a "1" slope in the log–log plot as changing the temporal resolution. Because of the

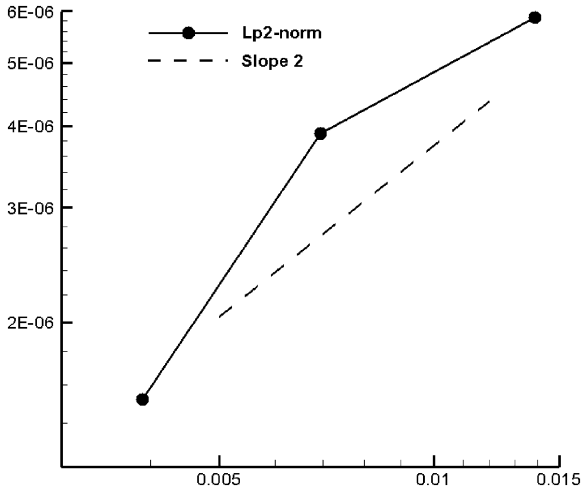

Fig. 3. The average value of l_{P2}-norm for three different mesh sizes conditions corresponding to $h=\frac{1}{72}$ cm, $\frac{1}{144}$ cm and $\frac{1}{256}$ cm ($\rho_P=1.25$ g/cm^3, $\mu=0.1$ g/(cm s), $\Delta t=3.125\times10^{-6}$ s).

Table 1
Comparisons of the maximum Reynolds number during the particle sedimentation for $\rho_P=1.25$ g/cm^3 and $\mu=0.1$ g(cm s)

$\rho_p=1.25$ g/cm^3, $\mu=0.1$ g/(cm s)							
	Present			Glowinski et al. (2001)		Wan and Turek (2007)	
h(cm)	$\frac{1}{72}$	$\frac{1}{144}$	$\frac{1}{256}$	$\frac{1}{192}$	$\frac{1}{256}$	$\frac{1}{48}$	$\frac{1}{96}$
Re_{Max}	16.962	17.216	17.307	17.27	17.31	17.42	17.15

Table 2
Comparisons of the maximum Reynolds number for different temporal increments ($\rho_P=1.25$ g/cm^3, $\mu=0.1$ g/(cm s), $h=\frac{1}{256}$ cm)

$\rho_P=1.25$ g/cm^3, $\mu=0.1$ g/(cm s), $h=\frac{1}{256}$ cm			
Δt (s)	5.0×10^{-5}	6.25×10^{-6}	3.125×10^{-6}
Re_{Max}	17.323	17.316	17.307

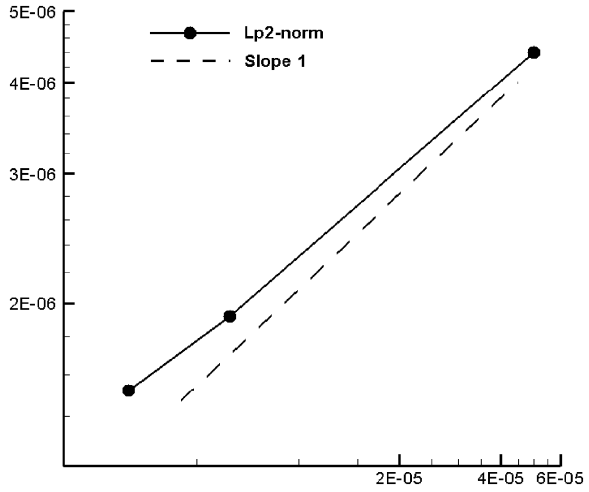

Fig. 4. Variation of average value of l_{P2}-norm at different temporal resolutions.

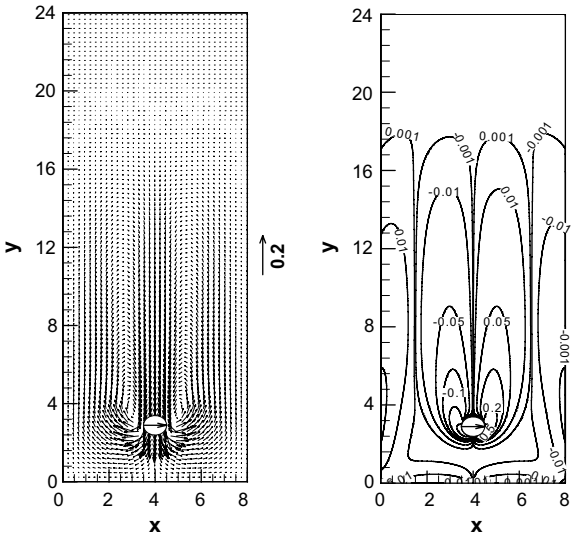

Fig. 5. Velocity vector (left) and vorticity contour (right) as well as the particle position at $t=0.687$ s for $\rho_P=1.25$ g/cm^3, $\mu=0.1$ g/(cm s), $h=\frac{1}{256}$ cm and $\Delta t=3.125\times10^{-6}$ s.

first order accuracy of solving the force exerted on a particle in Eq. (39), the temporal resolution of the simulation of particulate flow has first order accuracy. The velocity vector and vorticity contour as well as the particle position at $t = 0.687$ s during the sedimentation are demonstrated in Fig. 5. As can be seen that the flow field are highly symmetrical and no rotation happens to particle at this moment. The pressure distribution and the normal gradient of pressure at the particle surfaces at $t = 0.687$ s during the sedimentation are shown in Fig. 6. Under the effect of multi-direct forcing at the immersed boundary of the moving particle, there is a sharp variation of normal gradient of pressure at the particle surface (Fig. 6b) which indicates the good satisfaction of the no-slip condition there.

Fig. 7 shows the average value of l_{P2}-norm for different times of multi-directing forcing ($NF = 1$, 4, 10 and 20) for single particle sedimentation under the conditions of $\rho_P = 1.5$ g/cm^3, $\mu = 0.01$ g/(cm s), mesh size $h = \frac{1}{256}$ cm and time step $\Delta t = 3.125 \times 10^{-6}$ s. Once again, $NF = 1$ represents the original direct forcing scheme proposed by Fadlun et al. (2000) is applied at the immersed boundary of the particle, the average value of l_{P2}-norm is 1.685×10^{-2}. And the average value of l_{P2}-norm is 5.89×10^{-5} when the times of performing the multi-direct forcing is 20. As the increment of the times of performing the multi-direct forcing at the immersed boundary, the average value of l_{P2}-norm decreases in a near "−2" slope manner in the log–log plot. A better no-slip boundary condition at the immersed

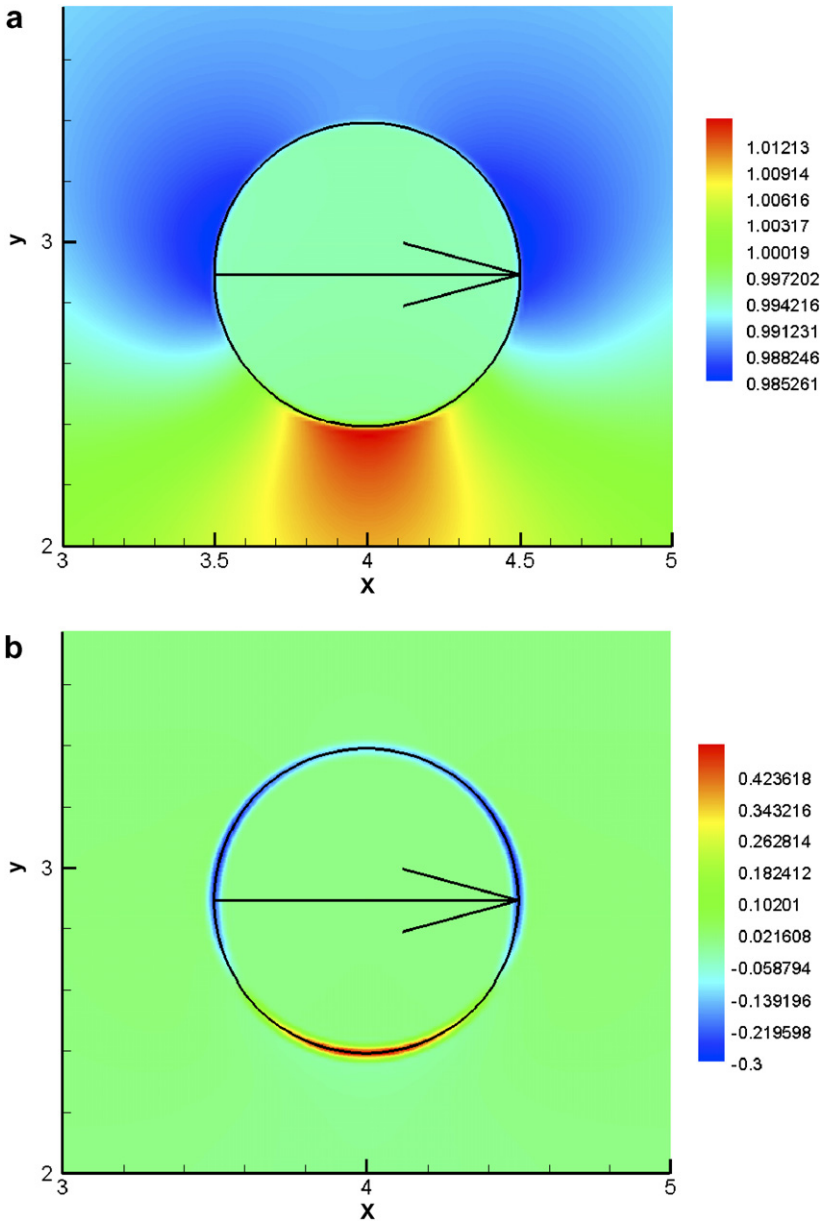

Fig. 6. Pressure distribution and the normal gradient of pressure at the particle surfaces at $t = 0.687$ s ((a) Pressure distribution; (b) normal gradient of pressure).

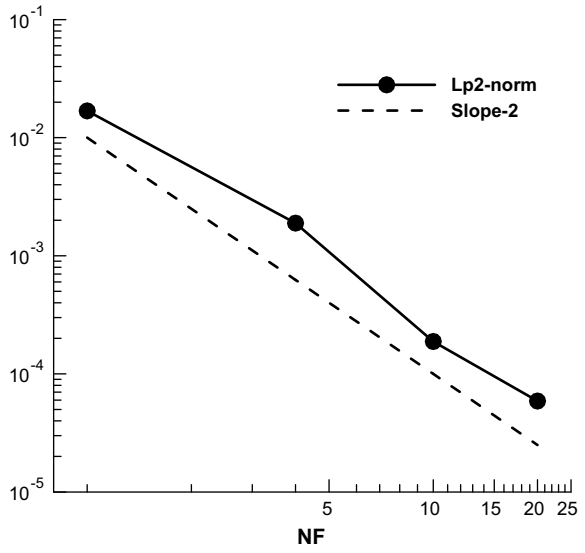

Fig. 7. The average value of l_{P2}-norm for different times of multi-directing forcing ($NF = 1$, 4, 10 and 20) for $\rho_P = 1.5$ g/cm^3, $\mu = 0.01$ g/(cm s), $h = \frac{1}{256}$ cm and $\Delta t = 3.125 \times 10^{-6}$ s.

boundary is reached as increasing the times of performing the multi-direct forcing scheme.

The maximum Reynolds numbers corresponding to the 1, 4, 10 and 20 times of performing the multi-direct forcing scheme for this case are 484.75, 500.61, 502.95 and 503.38, respectively. The 1-norm of the maximum Reynolds number is shown in Fig. 8 when NF increases from 1 to 20 with taking the maximum Reynolds number at $NF = 20$ as a base. The 1-norm of the maximum Reynolds number decreases in a "−2" slope manner in the log–log plot. As increasing the times of performing the multi-direct forcing at the immersed boundary of particle, the no-slip boundary condition of the particle is satisfied better, and a convergent result of the maximum Reynolds number for moving particle is obtained.

Fig. 9 shows time history of l_{P2}-norm for single particle sedimentation under the conditions of $\rho_P = 1.5$ g/cm^3, $\mu = 0.01$ g/(cm s), $NF = 20$, mesh size $h = \frac{1}{256}$ cm and time step $\Delta t = 3.125 \times 10^{-5}$ s corresponding to the maximum CFL number 0.107. Again, the l_{P2}-norm reduces to 5.89×10^{-5} soon and maintains this value during the whole simulation. And the average value of l_{P2}-norm for three different mesh sizes conditions corresponding to $h = \frac{1}{72}$ cm, $\frac{1}{144}$ cm and $\frac{1}{256}$ cm ($\rho_P = 1.5$ g/cm^3, $\mu = 0.01$ g/(cm s), $\Delta t = 3.125 \times 10^{-5}$ s, $NF = 20$) are shown in Fig. 10. The average values of l_{P2}-norm for $h = \frac{1}{72}$ cm and $\frac{1}{144}$ cm are 2.436×10^{-4} and 1.433×10^{-4}, respectively. And the average value of l_{P2}-norm varies in a "2" slope in the log–log plot as changing the resolution of mesh grid. A second order

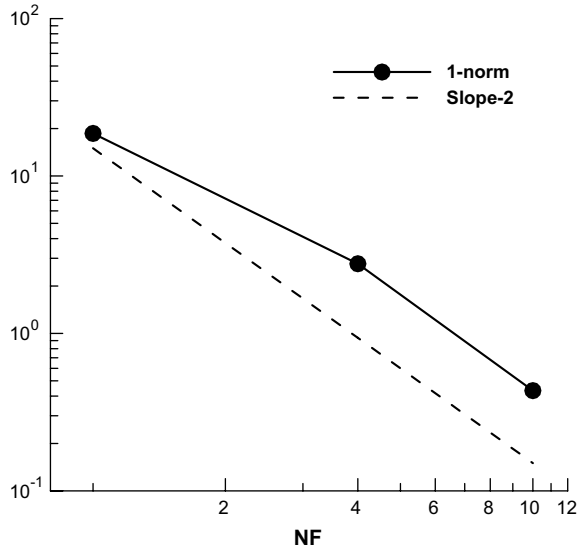

Fig. 8. Correlation between 1-norm of the maximum Reynolds number and the times of performing the multi-direct forcing for $\rho_P = 1.5$ g/cm^3, $\mu = 0.01$ g/(cm s), $h = \frac{1}{256}$ cm and $\Delta t = 3.125 \times 10^{-5}$ s with taking the maximum Reynolds number at $NF = 20$ as a base.

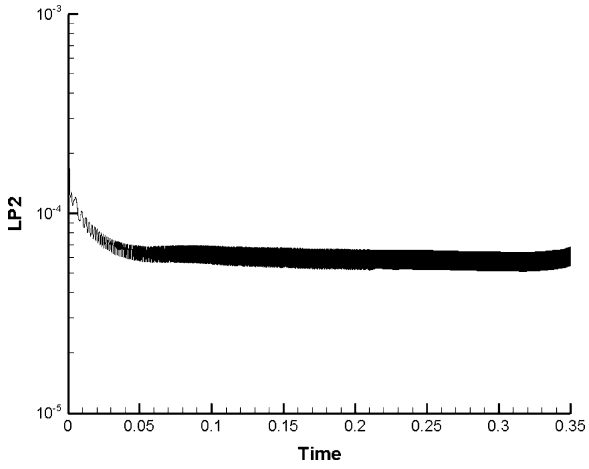

Fig. 9. Time history of l_{P2}-norm for $\rho_P = 1.5$ g/cm^3, $\mu = 0.01$ g/(cm s), $h = \frac{1}{256}$ cm and $\Delta t = 3.125 \times 10^{-5}$ s.

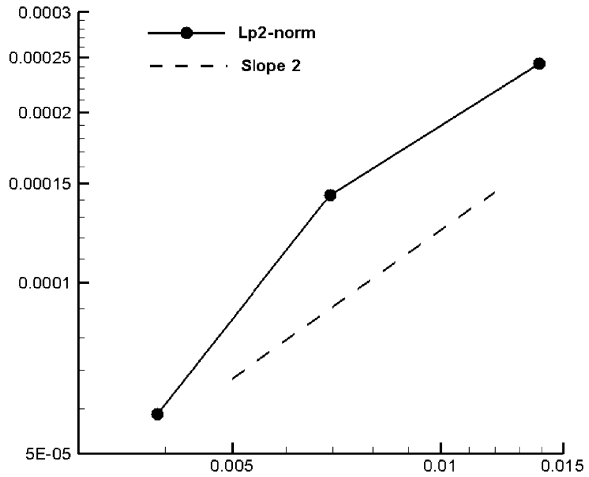

Fig. 10. The average value of l_{P2}-norm for three different mesh sizes conditions corresponding to $h = \frac{1}{72}$ cm, $\frac{1}{144}$ cm and $\frac{1}{256}$ cm ($\rho_P = 1.5$ g/cm^3, $\mu = 0.01$ g/(cm s), $\Delta t = 3.125 \times 10^{-5}$ s).

Table 3
Comparisons of the maximum Reynolds number during the particle sedimentation for $\rho_P = 1.5$ g/cm^3, $\mu = 0.01$ g/(cm s), and $\Delta t = 3.125 \times 10^{-5}$ s

$\rho_p = 1.5$ g/cm^3, $\mu = 0.01$ g/(cm s), $\Delta t = 3.125 \times 10^{-5}$ s									
	Present			Glowinski et al. (2001)			Wan and Turek (2007)		Uhlmann (2005)
h (cm)	$\frac{1}{72}$	$\frac{1}{144}$	$\frac{1}{256}$	$\frac{1}{192}$	$\frac{1}{256}$	$\frac{1}{384}$	$\frac{1}{48}$	$\frac{1}{96}$	$\frac{1}{256}$
Re_{Max}	502.37	503.26	503.38	438.6	450.7	466	442.19	465.52	495

accuracy for spacial resolution is obtained in present numerical simulation. The comparisons of the maximum Reynolds number during the particle settling in the fluid with previous numerical results under the same conditions are depicted in Table 3. In ours simulations, the maximum Reynolds number are 502.37, 503.27 and 503.38 for $h = \frac{1}{72}$ cm, $\frac{1}{144}$ cm and $\frac{1}{256}$ cm, respectively. The results are rough agreement with those of previous numerical simulations conducted by Glowinski et al. (2001) and Wan and Turek (2007), and are close to the results of numerical simulations done by Uhlmann (2004). Because the initial position of the particle is symmetric and the spatial discrete scheme keeps the symmetry, the perturbations grow very slow and the lateral offset of particle position is slightly, as shown in Fig. 11a. The evolution of vertical position of the particle center is shown in Fig. 11b. When the particle falls on the bottom, a colliding force is added on the particle and it rebounds back. It falls down and rebounds back alternately and finally the particle stays on the bottom of the rectangular domain as shown in Fig. 12. This is different from the simulation result conducted by Glowinski et al. (2001), but is more close to real physical observation. When the particle rebounds back, a pair of vortex is produced behind the bottom side of the particle (Fig. 12b). This pair of vortex encounters and combines the vortex at the top side of the particle (Fig. 12c). As this two pairs of vortex combination, these vortexes move to the side walls (Fig. 12d–e). When the particle re-hitting and rebounding to the lower wall, the same kind of vortex combination and expansion process is happened again but the intensity of vortex is much smaller (Fig. 12f).

Fig. 13 shows the velocity vector and vorticity contour as well as the particle position for $\rho_P = 1.5$ g/cm^3, $\mu = 0.01$ g/(cm s), $NF = 20$ and $h = \frac{1}{256}$ cm at $t = 0.338$ s. Due to the limited computational domain and symmetric computational algorithm, the pair of vortex behind the particle does not shed when the particle gets close to the bottom of the computational area. To observe the unstable dynamics behavior of vortex structures and particle behind the settling particle, we enlarge the computational domain to $\Omega = (0.2\text{ cm}) \times (0.15\text{ cm})$ to get a non-dimensional domain of $(0.8) \times (0.60)$ when taking the diameter of particle as the characteristic length. The initial position of particle is located at (1 cm,14 cm) (the non-dimensional position is (4, 56)). The diameter and density of the particle are 0.25 cm and 1.5 g/cm^3, respectively. The viscous of flow is $\mu = 0.01$ g/(cm s). The mesh size is $\frac{1}{36}$ of the particle diameter ($h = \frac{1}{144}$ cm). The temporal increment is $\Delta t = 3.125 \times 10^{-5}$ s. The times of performing the multi-direct forcing is $NF = 20$. The evolution process of flow field and particle position during single particle sedimentation is shown in Fig. 14. First, a pair of vortex is formed behind the particle and is lengthened as particle settling. Then, the pair of vortex is dislocated and sheds alternately due to the Helmholtz instability. As the vortex forms and sheds, the horizontal

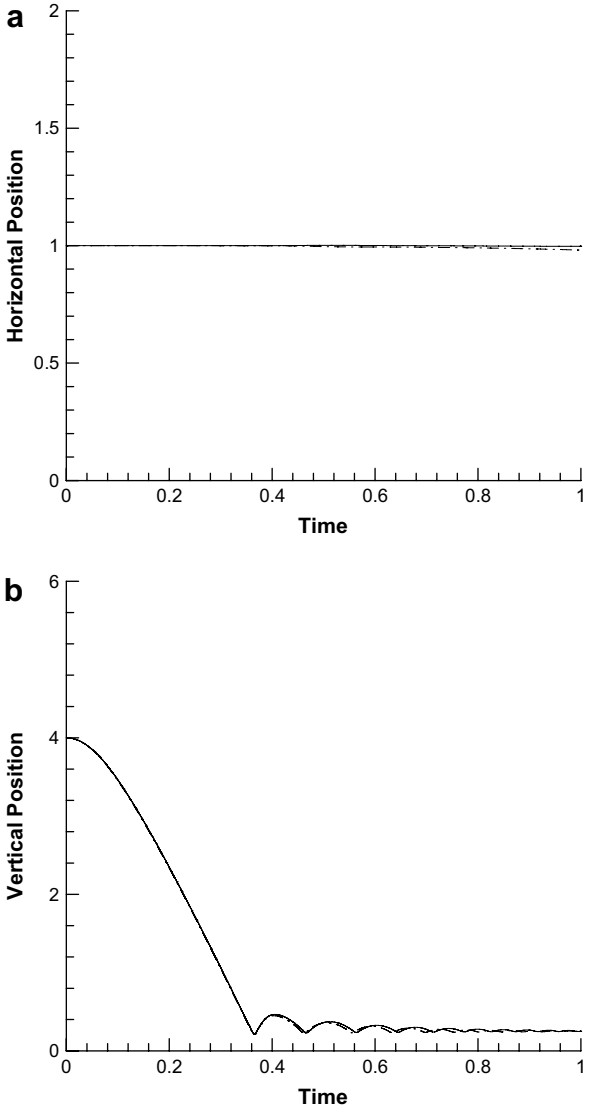

Fig. 11. Time history of the horizontal position (a) and the vertical position of the particle center (b) during the sedimentation for $\rho_P = 1.5$ g/cm^3 and $\mu = 0.01$ g/(cm s). $h = \frac{1}{144}$ cm: (—) solid line; $h = \frac{1}{256}$ cm: (-.-) dash-dot line.

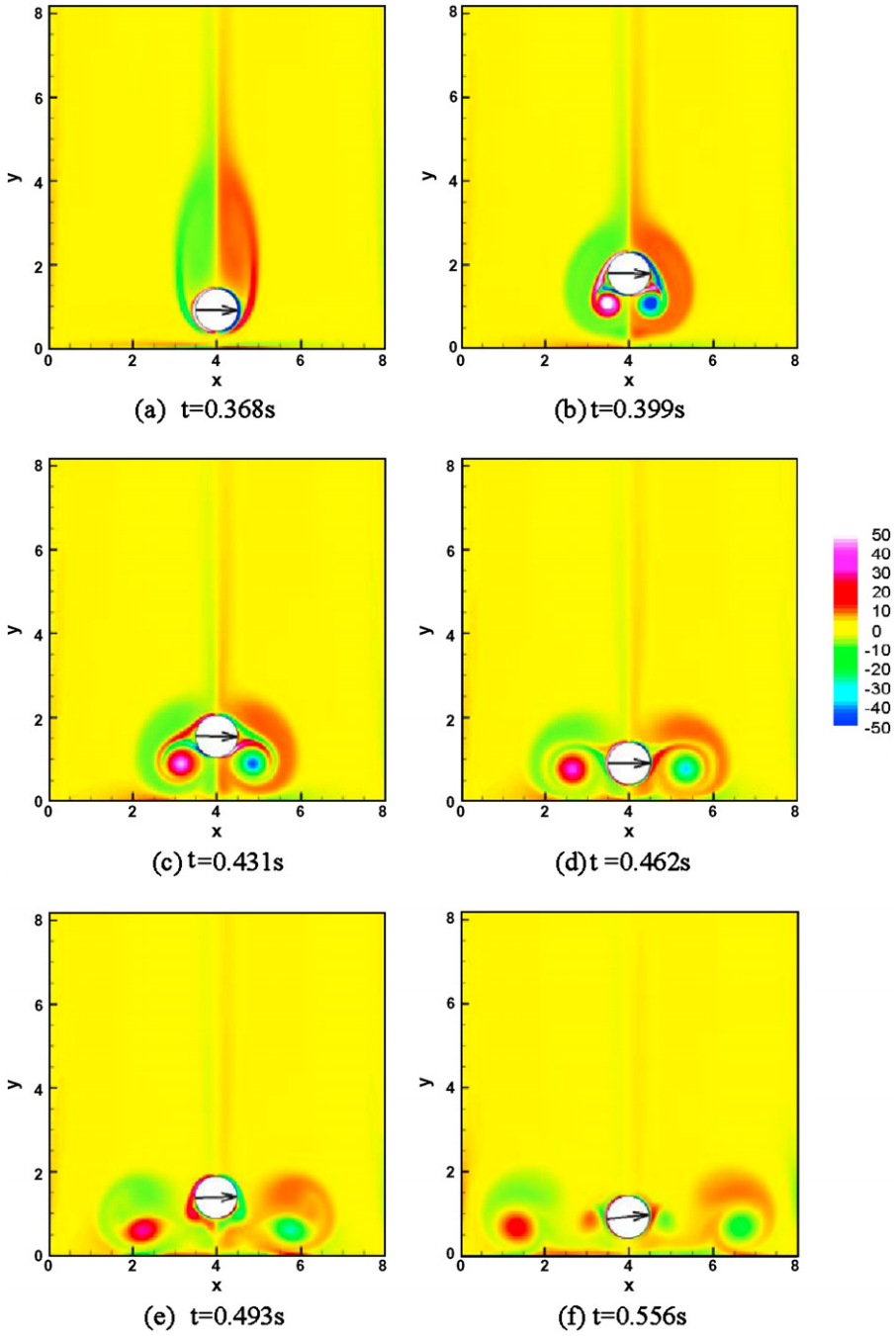

Fig. 12. Flow structure when particle reaches the lower wall for $\rho_P = 1.5$ g/cm^3, $\mu = 0.01$ g/(cm s), $h = \frac{1}{256}$ cm and $\Delta t = 3.125 \times 10^{-5}$ s.

position, the velocity and the angular velocity of the particle vary semi-periodically, as shown in Fig. 15. When the particle falls on the bottom, the vertical velocity and position get reverse due to a colliding force adding on the particle as shown in Fig. 15b and d. When the particle collide the lower wall in this case, the rotation of particle and the dislocated vortex let the particle move to a side of the wall with stronger rotating as shown in Fig. 16b. Large scale vortexes are broken up by the movement of particle (Fig. 16b and c), and the flow structures are totally different from those in Fig. 12. After a few times of hitting and rebounding, the particle stays on the bottom of the computational domain.

3.2. Drafting, kissing and tumbling of two settling particles

The drafting–kissing–tumbling phenomenon has been studied extensively. The leading particle creates a wake of low pressure, and the trailing particle is caught in its wake which reduces the drag in the trailing one and falls faster

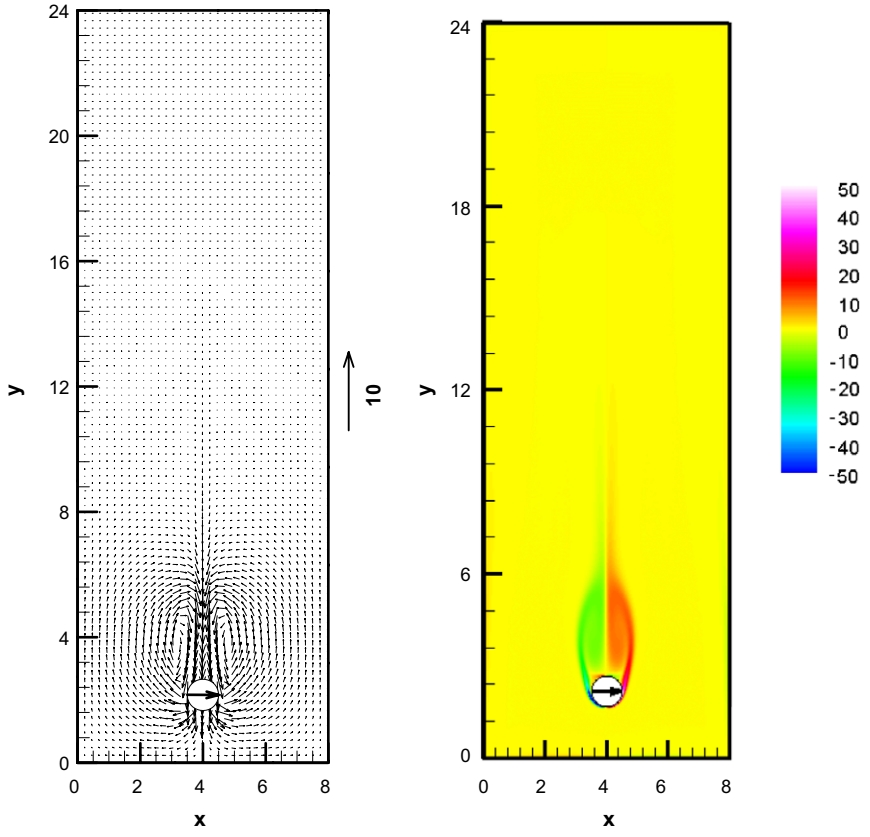

Fig. 13. Velocity vector (left) and vorticity contour (right) as well as the particle position at $t = 0.338$ s for $\rho_P = 1.5$ g/cm^3 and $\mu = 0.01$ g/(cm s), $h = \frac{1}{256}$ cm and $\Delta t = 3.125 \times 10^{-5}$ s.

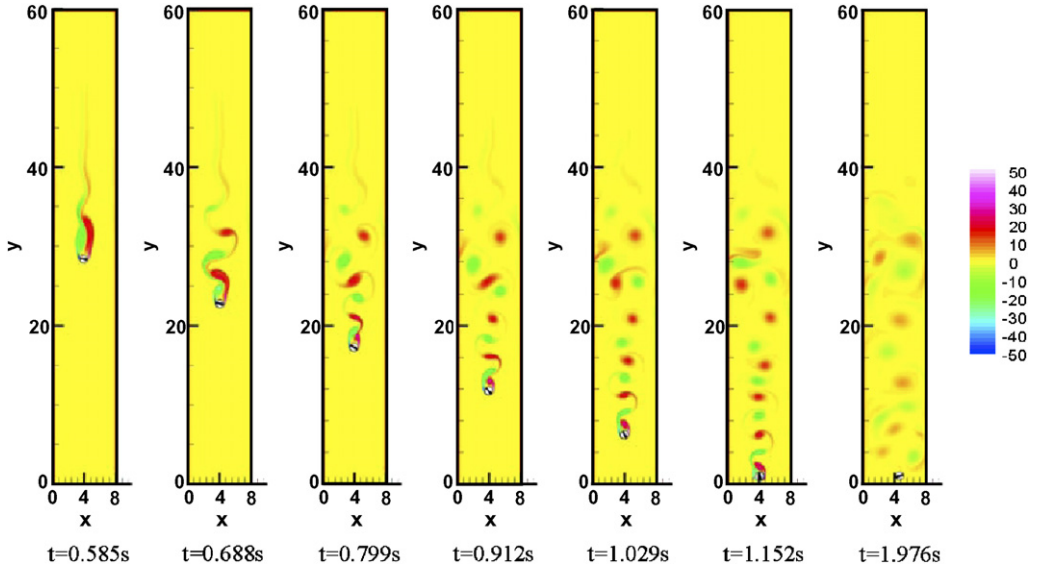

Fig. 14. Evolution process of flow field and particle position during the particle sedimentation for $\rho_P = 1.5$ g/cm^3, $\mu = 0.01$ g/(cm s) and $h = \frac{1}{144}$ cm.

than the leading one. The increased speed of the trailing particle impels a kissing contact with the leading one. The two particles form a long body with the line of center along the stream. This is an unstable equilibrium state. If there is a small perturbation, the equilibrium state is broken down and the particles tumble until another equilibrium state is reached. Here, we use the immersed boundary method with multi-direct forcing to solve this problem.

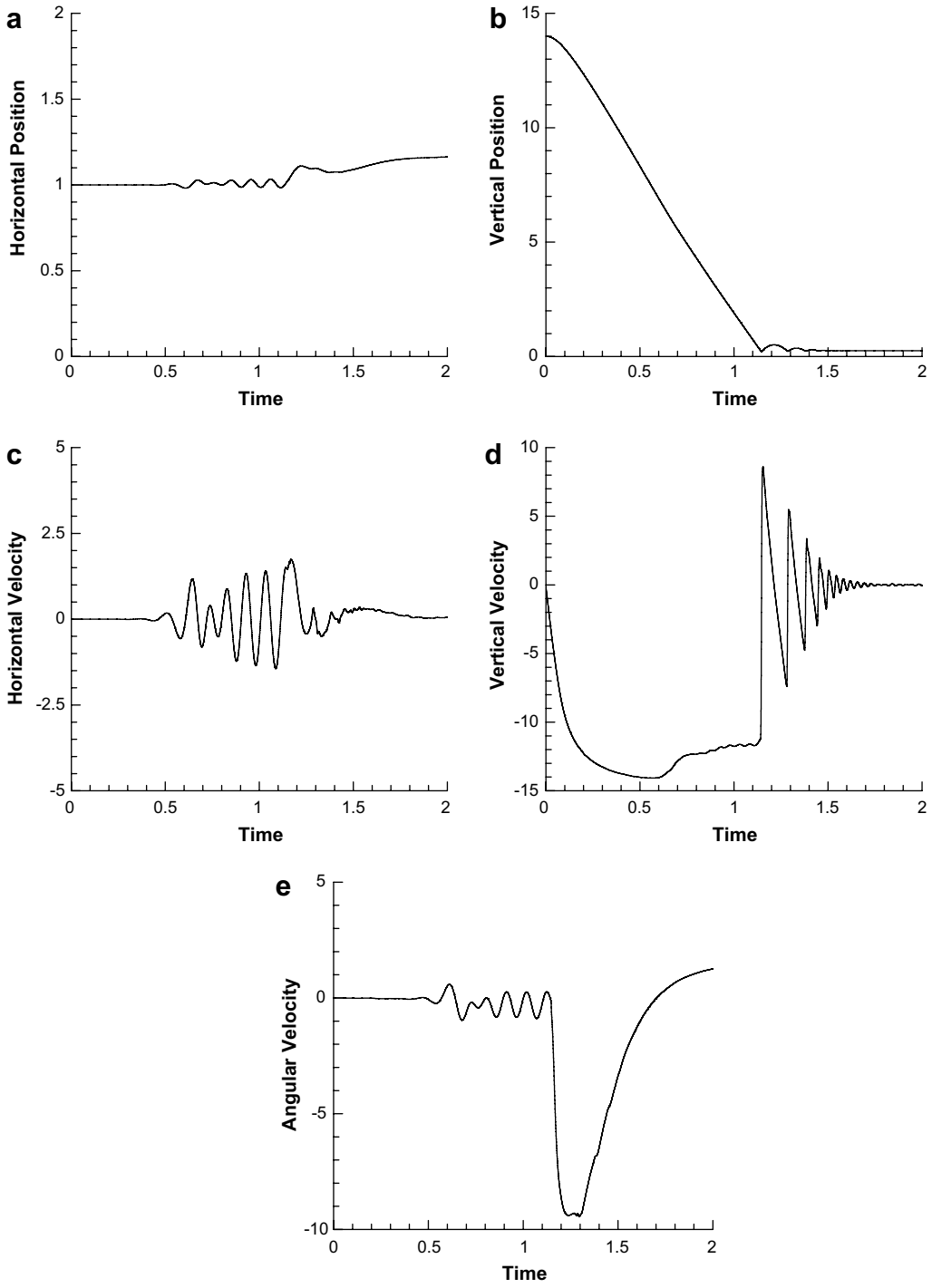

Fig. 15. Evolution of the horizontal position of particle (a), vertical position of particle (b), horizontal velocity of particle (c), vertical velocity (d) and angular velocity (e) during the particle settling for $\rho_P = 1.5$ g/cm^3, $\mu = 0.01$ g/(cm s) and $h = \frac{1}{144}$ cm.

3.2.1. Results by immersed boundary method with multi-direct forcing

The computational parameters are summarized as follows:
The computational domain is $\Omega = (0.2\text{ cm}) \times (0.2\text{ cm})$.
The diameter of the particle is $D_P = 0.25$ cm.
The density of the particle is $\rho_P = 1.5$ g/cm^3.
The center of the particle is located at $(1 - 0.001\text{ cm}, 4.5\text{ cm})$ and $(1 + 0.001\text{ cm}, 5\text{ cm})$ at time $t = 0$
The fluid and the particle are initially at rest.
The fluid density is $\rho_f = 1.00$ g/cm^3.
The fluid viscous is $\mu = 0.01$ g/(cm s).
The collision parameter is $\varepsilon_P = \varepsilon'_P = 1.0 \times 10^{-7}$, $\varepsilon_W = 0.5\varepsilon_P$, and the force range $\xi = 2h$, where h is the mesh size.

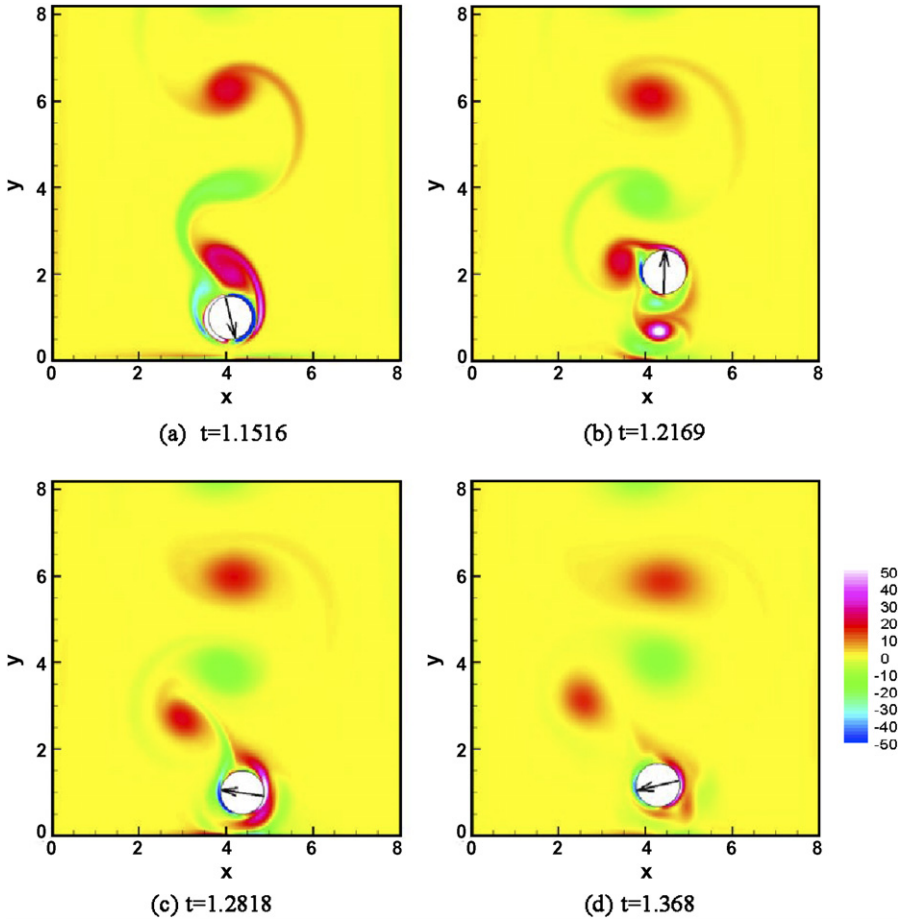

Fig. 16. Flow structure when particle reaches the lower wall for $\rho_P = 1.5$ g/cm^3, $\mu = 0.01$ g/(cm s) and $h = \frac{1}{144}$ cm.

The mesh size is $\frac{1}{64}$ of the particulate diameter ($h = \frac{1}{256}$ cm). The temporal increment is $\Delta t = 6.25 \times 10^{-5}$ s. The multi-direct forcing is performed for $NF = 20$ times and 202 Lagrangian points are used at the immersed boundary.

The initial horizontal positions of the two particles are set non-symmetric to accelerate the growth of perturbations. Otherwise, only drafting and kissing can be observed and the tumbling could not happen. This is because the symmetric computational algorithm lead the perturbations grow slowly and the small perturbation cannot break down the equilibrium state when the two particles collide as discussed in Uhlmann (2005). The kissing and tumbling stages are sensitive to the choice of initial horizontal positions of the two particles.

Fig. 17 shows the time histories of horizontal positions and vertical positions of the two particles for $\rho_P = 1.5$ g/cm^3 and $\mu = 0.01$ g/(cm s). The variation trends of horizontal positions for the two particles are the same, but the vertical positions of two particles cross each other, which suggest that the drafting, kissing and tumbling happen for the two settling particles. The time histories of the horizontal velocities and vertical velocities of the two particles are depicted in Fig. 18. The crossing of the particle velocities also indicates the happening of the drafting, kissing and tumbling phenomenon. Fig. 19 shows the histories of the angular velocities of the two particles under the same conditions as above. As can be seen that the magnitude of the angular velocities for the two particles are close to each other, but the rotating directions are opposite. Fig. 20 shows the positions of particles and the vorticity contour in the flow of two particle sedimentation at different time for $\rho_P = 1.5$ g/cm^3, $\mu = 0.01$ g/(cm s) and $h = \frac{1}{256}$ cm. Clearly, the drafting, kissing and tumbling (DKT) phenomenon is successfully reproduced. The trailing particle is caught by the low-pressure wake created by the leading particle, then the drag acted on it is reduced and it falls faster than the leading one. The increased speed of the trailing particle impels a kissing contact with the leading one. If there is a small perturbation, this equilibrium state is broken down and the particles tumble happens. The opposite rotating directions are also clearly indicated by the arrow marked on the particles. These results are consistent with many previous experimental and numerical results (Hu, 1996; Hu et al., 2001; Glowinski et al., 1999; Glowinski et al., 2001; Patankar et al., 2000; Sharma and Patankar, 2005; Perrin and Hu, 2006). At the colliding moment of the two particles, a jet flow is observed in between the

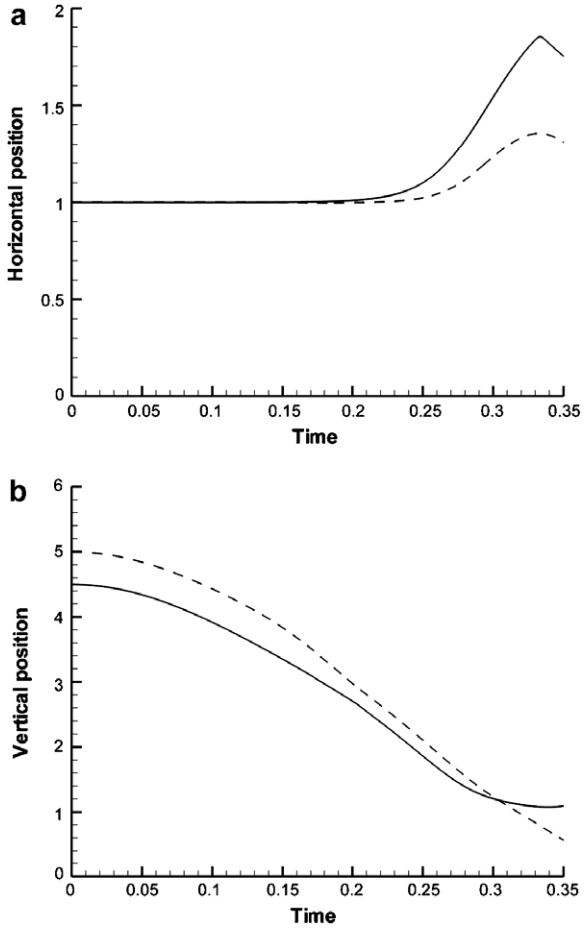

Fig. 17. Time history of the horizontal positions (a) and vertical positions (b) of the center of the particles for $\rho_P = 1.5$ g/cm^3, $\mu = 0.01$ g/(cm s) and $h = \frac{1}{256}$ cm. leading: (—) solid line, trailing: (---) dashed line.

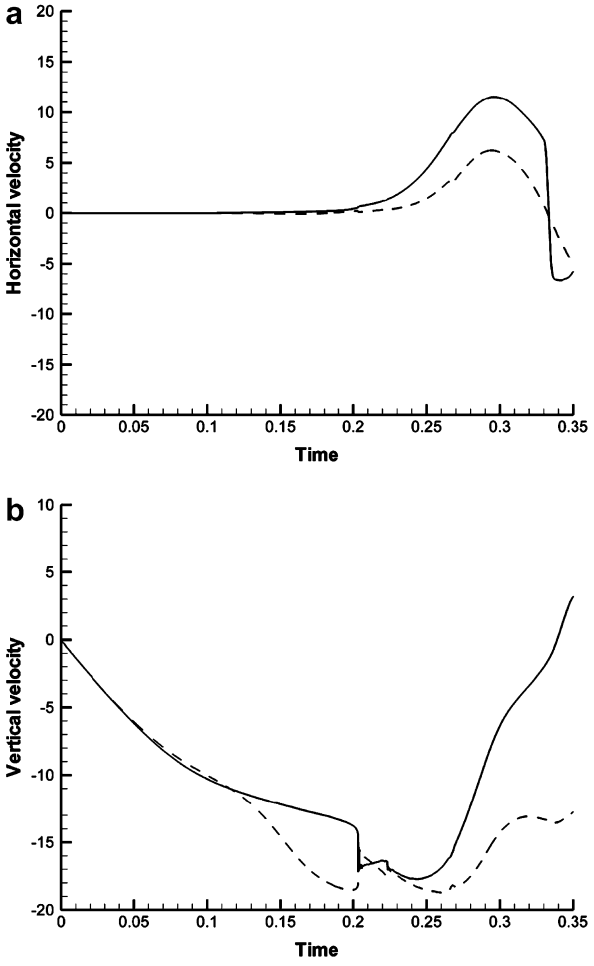

Fig. 18. Time histories of the horizontal velocities (a) and vertical velocities (b) of the two particles for $\rho_P = 1.5$ g/cm^3, $\mu = 0.01$ g/(cm s) and $h = \frac{1}{256}$ cm. leading: (—) solid line, trailing: (---) dashed line.

two particles in the transverse direction to the hitting as shown in Fig. 21.

3.2.2. *Quantitatively comparison with the results of Feng and Michaelides (2004)*

In order to make comparison quantitatively, we compare the results obtained by present immersed boundary method with multi-direct forcing scheme with the results from Feng and Michaelides (2004) who applied the immersed boundary-lattice Boltzmann method to solve fluid–particles interaction problems including the DKT case. Here, all the computational parameters are the same as those in Feng and Michaelides (2004) except the collision parameters due to different collision strategy. And these computational parameters are presented as follow:

The computational domain is $\Omega = (0.2\text{ cm}) \times (0.8\text{ cm})$.
The diameter of the particle is $D_P = 0.2$ cm.
The density of the particle is $\rho_P = 1.01$ g/cm^3.
The center of the particle is located at (1 cm, 6.8 cm) and $(1 - 0.001\text{ cm}, 7.2\text{ cm})$ at time $t = 0$.
The fluid and the particle are initially at rest.

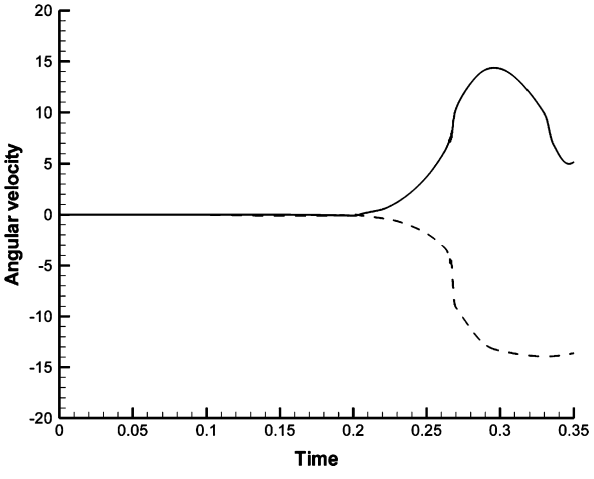

Fig. 19. Time histories of the angular velocities of the particles for $\rho_P = 1.5$ g/cm^3, $\mu = 0.01$ g/(cm s) and $h = \frac{1}{256}$ cm. leading: (—) solid line, trailing: (---) dashed line.

The fluid density is $\rho_f = 1.00$ g/cm^3.
The fluid viscous is $\mu = 0.001$ g/(cm s).

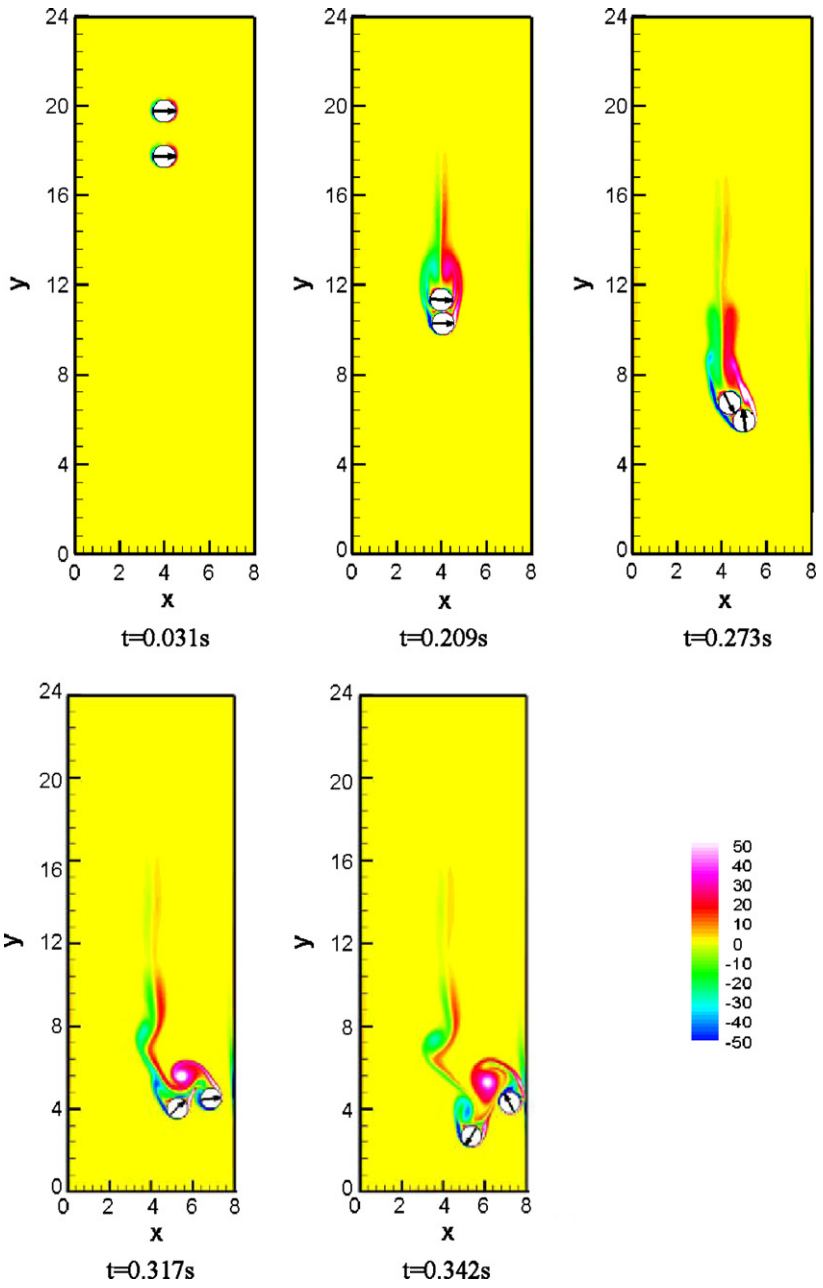

Fig. 20. Positions of particles and vorticity contour for DKT at different times for $\rho_P = 1.5$ g/cm^3, $\mu = 0.01$ g/(cm s) and $h = \frac{1}{256}$ cm.

The collision parameter is $\varepsilon_P = \varepsilon'_P = 1.0 \times 10^{-7}$, $\varepsilon_W = 0.5\varepsilon_P$, and the force range $\xi = 2h$, where h is the mesh size.

The mesh size is $\frac{1}{30}$ of the particulate diameter ($h = \frac{1}{150}$ cm). The temporal increment is $\Delta t = 5.0 \times 10^{-4}$ s. The multi-direct forcing is performed for $NF = 20$ times and 96 Lagrangian points are used at the immersed boundary.

Fig. 22 shows the time histories of vertical velocities of the two particles and the results by Feng and Michaelides (2004). The drafting, and kissing part of the process agree with the results by Feng and Michaelides (2004) very well, and the tumbling part especially for the separation of the two particles is different from that of Feng and Michaelides (2004) for applying different collision strategy between particles in the simulation. Therefore, the results of DKT process with immersed boundary method and multi-direct forcing scheme agree very well with the results obtained by immersed boundary-lattice Boltzmann method (Feng and Michaelides, 2004) quantitatively.

3.3. Sedimentation of hundreds of particles

Sedimentation of one hundred and five particles in a close domain is also simulated to check the availability of

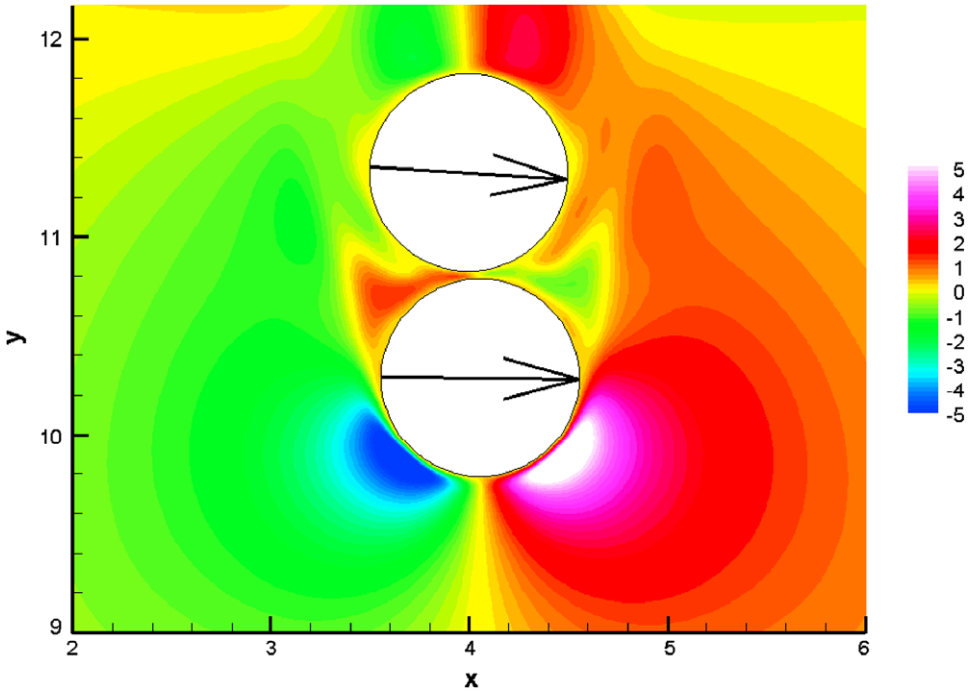

Fig. 21. Horizontal velocity distribution for DTK at the moment of two particle kissing ($\rho_P = 1.5$ g/cm^3, $\mu = 0.01$ g/(cm s) and $h = \frac{1}{256}$ cm). A jet flow is generated in between particles in the transverse direction to the hitting.

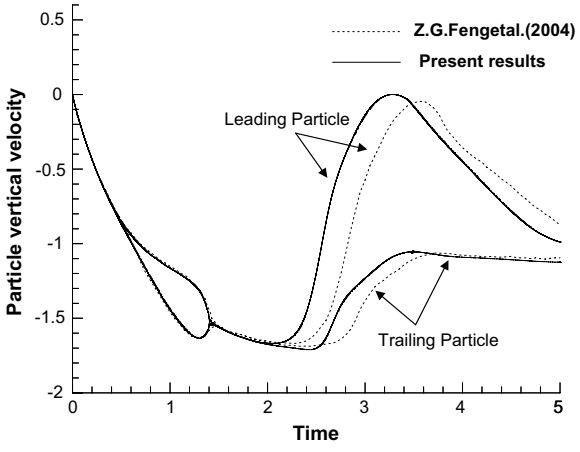

Fig. 22. Time histories of vertical velocities of two particles and the results by Feng and Michaelides (2004) ($\rho_P = 1.01$ g/cm^3, $\mu = 0.001$ g/(cm s) and $h = \frac{1}{150}$ cm).

applying the multi-direct forcing technique to study many-body motion. The computational parameters are summarized as follows:

The diameter of the particle is $D_P = 0.25$ cm.
The density of the particle is $\rho_P = 1.5$ g/cm^3.
The fluid and the particle are initially at rest.
The fluid density is $\rho_f = 1.00$ g/cm^3.
The fluid viscous is $\mu = 0.01$ g/(cm s).
The collision parameter is $\varepsilon_P = \varepsilon'_P = 1.0 \times 10^{-7}$, $\varepsilon_W = 0.5\varepsilon_P$, and the force range $\xi = 2h$, where h is the mesh size.

The mesh size is $\frac{1}{18}$ of the particle diameter, i. e. $h = \frac{1}{72}$ cm. The temporal increment is $\Delta t = 6.25 \times 10^{-5}$ s. The multi-direct forcing is performed for $NF = 20$ times and 57 Lagrangian points are used at the immersed boundary.

Fig. 23 demonstrates the temporal evolution of the particle positions and flow structures in the close domain. The particles are initially arranged in the top region of the computational domain. It is found that the dense particles fall down under the influence of gravity and two vortices forms near the two top corners at the first, as shown in Fig. 23b and c. The particles near two-side walls fall down quickly but the particles in the middle of the domain are held by the fluid, as shown in Fig. 23d and e. During the sedimentation of particles, a bubble of fluid is formed with particles around. When the particles settle down on the bottom of the computational domain, the particles gather together in the middle region of the closed domain from two sides of the bubble, as shown in Fig. 23f and g. At the end, all the particles settle down and stay on the bottom of the closed domain. These complex dynamics characteristics are also successfully captured in the present study, which confirms the reliability of applying the proposed multi-direct forcing to flows laden with moving particles.

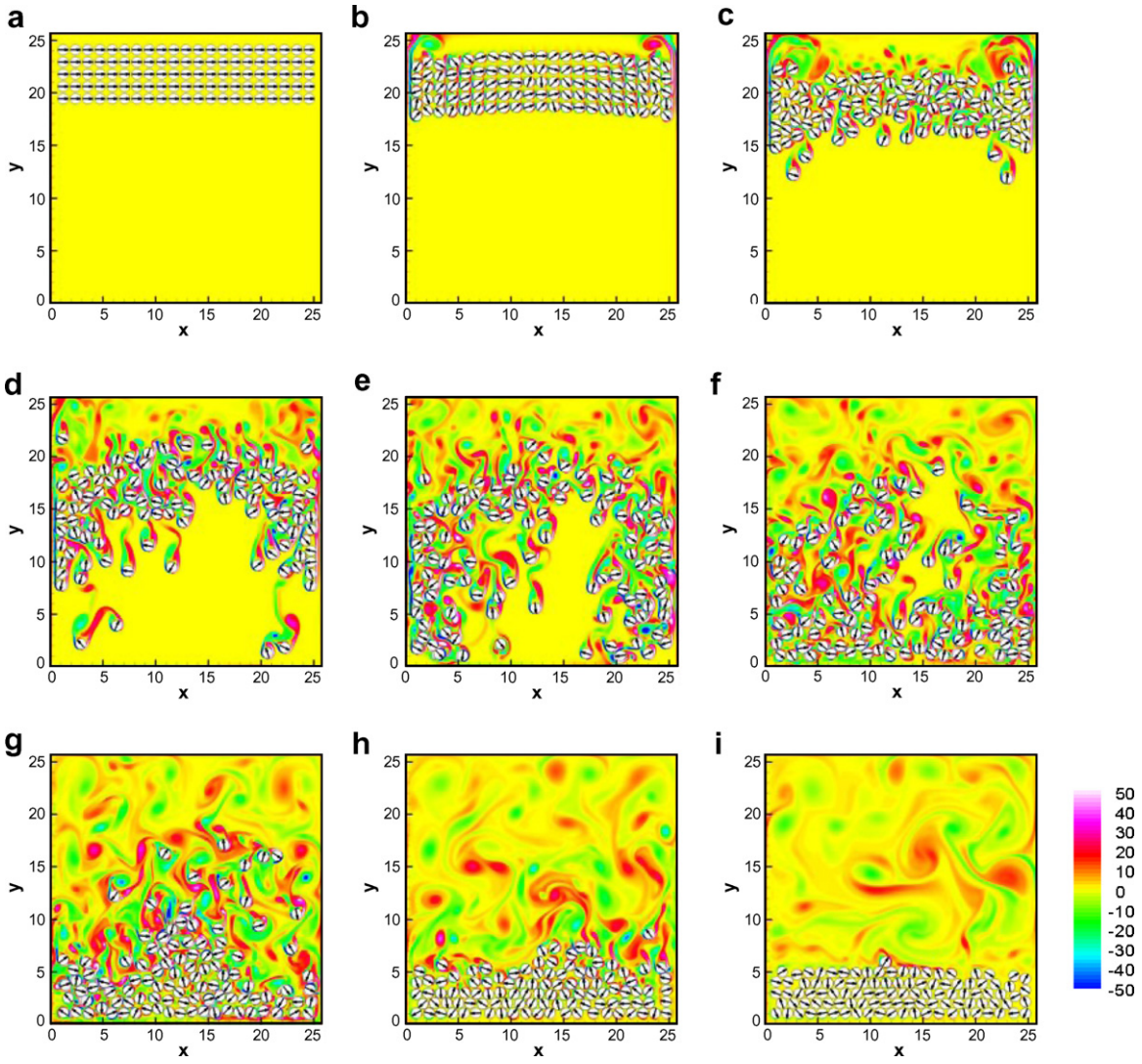

Fig. 23. Sedimentation process of 105 particles in a close domain.

4. Summary and conclusion

The *multi-direct forcing* scheme, proposed for calculation of the hydrodynamic interactions between rigid boundary and fluid, is applied to simulate flows laden with moving particles. Compared with the original direct forcing scheme proposed by Fadlun et al. (2000), the multi-direct forcing scheme can obtain a better no-slip boundary condition at the immersed boundary. That the sedimentation of a single particle in a channel under different conditions and the sedimentation of two particles in a channel as well as the sedimentation of 105 particles in a close domain is numerically simulated using the multi-direct forcing technique combined with immersed boundary method. Some microcosmic phenomena, such as the hitting and rebounding of the single particle sedimentation, the drafting–kissing–tumbling of two settling particles and sedimentation of many particles are successfully captured. The tracked l_{P2}-norm and the quantitative agreement of the maximum Reynolds number during the particle sedimentation and the DKT phenomenon with other studies also prove that the present combined multi-direct forcing and immersed boundary method can be used to effectively simulate particle-laden flows with full-scale solutions.

Acknowledgements

This work is supported by the National Natural Science Foundation of China (No. 50506027, No. 50736006) and Zhejiang Provincial Natural Science Foundations of China (No. Z104314). We are grateful to that.

References

Barré, C., Mashayek, F., Taulbee, D.B., 2001. Statistics in particle-laden plane strain turbulence by direct numerical simulation. Int. J. Multiphase Flow 27, 347–378.

Biswas, S., Esmaeeli, A., Tryggvason, G., 2005. Comparison of results from DNS of bubbly flows with a two-fluid model for two-dimensional laminar flows. Int. J. Multiphase Flow 31, 036–1048.

Burton, T.M., Eaton, J.K., 2005. Fully resolved simulations of particle–turbulence interaction. J. Fluid Mech. 545, 67–111.

Cho, S.H., Choi, H.G., Yoo, J.Y., 2005. Direct numerical simulation of fluid flow laden with many particles. Int. J. Multiphase Flow 31, 435–451.

Fadlun, E.A., Verzicco, R., Orlandi, P., Mohd-Yusof, J., 2000. Combined immersed-boundary finite-difference methods for three-dimensional complex flow simulations. J. Comput. Phys. 161, 35–60.

Fan, J.R., Luo, K., Ha, M.Y., Cen, K.F., 2004. Direct numerical simulation of a near field particle-laden plane turbulent jet. Phys. Rev. E 70, 026303.

Feng, Z.G., Michaelides, E.E., 2004. The immersed boundary-lattice Boltzmann method for solving fluid-particles interaction problems. J. Comput. Phys. 195, 602–628.

Ferrante, A., Elghobashi, S., 2003. On the physical mechanisms of two-way coupling in particle-laden isotropic turbulence. Phys. Fluids 15, 315–329.

Glowinski, R., Pan, T.W., Hesla, T.I., Joseph, D.D., 1999. A distributed Lagrange multiplier/fictitious domain method for particulate flows. Int. J. Multiphase Flow 25, 755–794.

Glowinski, R., Pan, T.W., Hesla, T.I., Joseph, D.D., Périaux, J., 2001. A fictitious domain approach to the direct numerical simulation of incompressible viscous flow past moving rigid bodies: application to particulate flow. J. Comput. Phys. 169, 363–426.

Goldstein, D., Handler, R., Sirovich, L., 1993. Modeling a no-slip boundary with an external force field. J. Comput. Phys. 105, 354–366.

Gore, R.A., Crowe, C.T., 1989. Effect of particle size on modulating turbulent intensity. Int. J. Multiphase Flow 15, 279–285.

Griffith, B.E., Peskin, C.S., 2005. On the order of accuracy of the immersed boundary method: higher order convergence rates for sufficiently smooth problems. J. Comput. Phys. 208, 75–105.

Hetsroni, G., 1989. Particle–turbulence interaction. Int. J. Multiphase Flow 15, 735–746.

Hu, H.H., 1996. Direct simulation of flows of solid–liquid mixtures. Int. J. Multiphase Flow 22, 335–352.

Hu, H.H., Patankar, N.A., Zhu, N., 2001. Direct numerical simulation of fluid–solid systems using the arbitrary Lagrangian Eulerian technique. J. Comput. Phys. 169, 427–462.

Jameson, A., Schmidt, W., 1985. Some recent development in numerical methods for transonic flow. Comput. Methods Appl. Mech. Eng. 51, 467–493.

Kajishima, T., Takiguchi, S., 2002. Interaction between particle clusters and particle-induced turbulence. Int. J. Heat Fluid Flow 23, 639–646.

Ladd, A.J.C., Verberg, R., 2001. Lattice–Boltzmann simulation of particle–fluid suspensions. J. Stat. Phys. 104, 1191–1251.

Lele, S.K., 1992. Compact finite difference scheme with spectral-like resolution. J. Comput. Phys. 103, 16–42.

Ling, W., Chung, J.N., Troutt, T.R., Crowe, C.T., 1998. Direct numerical simulation of a three-dimensional temporal mixing layer with particle dispersion. J. Fluid Mech. 358, 61–85.

Lomholt, S., Stenum, B., Maxey, M.R., 2002. Experimental verification of the force coupling method for particulate flows. Int. J. Multiphase Flow 28, 225–246.

Luo, K., Klein, M., Fan, J.R., Cen, K.F., 2006. Effect on particle dispersion by turbulent transition in a jet. Phys. Lett. A 357, 345–350.

Marchioli, C., Giusti, A., Salvetti, M.V., Soldati, A., 2003. Direct numerical simulation of particle wall transfer and deposition in upward turbulent pipe flow. Int. J. Multiphase Flow 29, 1017–1038.

Maxey, M.R., Patel, B.K., 2001. Localized force representations for particles sedimenting in Stokes flow. Int. J. Multiphase Flow 27, 1603–1626.

Mittal, R., Iaccarino, G., 2005. Immersed boundary methods. Annu. Rev. Fluid Mech. 37, 239–261.

Moin, P., Mahesh, K., 1998. Direct numerical simulation: a tool in turbulence research. Annu. Rev. Fluid Mech. 30, 539–578.

Pan, T.W., Joseph, D.D., Glowinski, R., 2001. Modeling Rayleigh–Taylor instability of a sedimenting suspension of several thousand circular particles in direct numerical simulation. J. Fluid Mech. 434, 23–37.

Pan, Y., Tanaka, T., Tsuji, Y., 2002a. Turbulence modulation by dispersed solid particles in rotating channel flows. Int. J. Multiphase Flow 28, 527–552.

Pan, T.W., Joseph, D.D., Bai, R., Glowinski, R., Sarin, V., 2002b. Fluidization of 1204 spheres: simulation and experiment. J. Fluid Mech. 451, 169–191.

Patankar, N.A., Joseph, D.D., 2001. Modeling and numerical simulation of particulate flows by the Eulerian–Lagrangian approach. Int. J. Multiphase Flow 27, 1659–1684.

Patankar, N.A., Singh, P., Joseph, D.D., Glowinski, R., Pan, T.W., 2000. A new formulation of the distributed Lagrange multiplier/fictitious domain method for particulate flows. Int. J. Multiphase Flow 26, 1509–1524.

Patankar, N.A., Joseph, D.D., Wang, J., Barree, R.D., Conway, M., Asadi, M., 2002. Power law correlations for sediment transport in pressure driven channel flows. Int. J. Multiphase Flow 28, 1269–1292.

Pedinotti, S., Mariotti, G., Banerjee, S., 1992. Direct numerical simulation of particle behaviour in the wall region of turbulent flows in horizontal channels. Int. J. Multiphase Flow 18, 927–941.

Perrin, A., Hu, H.H., 2006. An explicit finite-difference scheme for simulation of moving particles. J. Comput. Phys. 212, 166–187.

Peskin, C.S., 1972. Flow patterns around heart valves: a numerical method. J. Comput. Phys. 10, 252.

Prosperetti, A., Oguz, H.N., 2001. Physalis: A new O(N) method for the numerical simulation of disperse systems: Potential flow of spheres. J. Comput. Phys. 167, 196–216.

Saiki, E.M., Biringen, S., 1996. Numerical simulation of a cylinder in uniform flow: application of a virtual boundary method. J. Comput. Phys. 123, 450–465.

Scardovelli, R., Zaleski, S., 1999. Direct numerical simulation of free-surface and interfacial flow. Ann. Rev. Fluid Mech. 31, 567.

Sharma, N., Patankar, N.A., 2005. A fast computation technique for the direct numerical simulation of rigid particulate flows. J. Comput. Phys. 205, 439–457.

Silva, A.L.F.L.E., Silveira-Neto, A., Damasceno, J.J.R., 2003. Numerical simulation of two-dimensional flows over a circular cylinder using the immersed boundary method. J. Comput. Phys. 189, 351–370.

Singh, P., Hesla, T.I., Joseph, D.D., 2003. Distributed Lagrange multiplier method for particulate flows with collisions. Int. J. Multiphase Flow 29, 495–509.

Soltani, M., Ahmadi, G., Ounis, H., McLaughlin, J.B., 1998. Direct simulation of charged particle deposition in a turbulent flow. Int. J. Multiphase Flow 24, 77–92.

Squires, K.D., Eaton, J.K., 1990. Particle response and turbulence modification in isotropic turbulence. Phys. Fluids A 2, 1191–1203.

Sussman, M., Smereka, P., Osher, S., 1994. A level set approach for computing solutions to incompressible two-phase flows. J. Comput. Phys. 114, 146.

Takagi, S., Oguz, H.N., Zhang, Z., Prosperetti, A., 2003. PHYSALIS: a new method for particle simulation Part II: two-dimensional Navier–Stokes flow around cylinders. J. Comput. Phys. 187, 371–390.

Tryggvason, G., Bunner, B., Esmaeeli, A., Juric, D., Al-Rawahi, N., Tauber, W., Han, J., Nas, S., Jan, Y.-J., 2001. A front-tracking method for the computations of multiphase flow. J. Comput. Phys. 169, 708–759.

Tsuji, Y., Morikawa, Y., 1982. LDV measurements in air-solid two-phase flow in a vertical pipe. J. Fluid Mech. 139, 417–434.

Tsuji, Y., Morikawa, Y., Shiomi, H., 1984. LDV measurements of an air-solid two-phase flow in a vertical pipe. J. Fluid Mech. 139, 417–434.

Uhlmann, M., 2004. Numerical simulation of particulate flows: comparison of fictitious domain methods with direct. and indirect forcing. In: Andersson, H.I., Krogstad, P.-A., Advances in Turbulence X, Proceedings of 10th European Turbulence Conference, pp. 415–418.

Uhlmann, M., 2005. An immersed boundary method with direct forcing for the simulation of particulate flows. J. Comput. Phys. 209, 448–476.

Wan, D., Turek, S., 2007. An efficient multigrid-FEM method for the simulation of solid–liquid two phase flows. J. Comput. Appl. Math. 203, 561–580.

Yabe, T., Xiao, F., Utsumi, T., 2001. The constrained interpolation profile (CIP) method for multiphase analysis. J. Comput. Phys. 169, 556.

Zhang, Z., Prosperetti, A., 2003. A method for particle simulation. J. Appl. Mech.-Trans. ASME 70, 64–74.